S-CHAIN: STRUCTURED VISUAL CHAIN-OF-THOUGHT FOR MEDICINE

Anonymous authors

000

001

002003004

006

008 009

010

011

012

013

014

015

016

017

018

019

021

024

025 026 027

028 029

031

033

034

035

037

040

041

042

043

044

045

046

047

048

051

052

Paper under double-blind review

ABSTRACT

Faithful reasoning in medical vision-language models (VLMs) requires not only accurate predictions but also transparent alignment between textual rationales and visual evidence. While Chain-of-Thought (CoT) prompting has shown promise in medical visual question answering (VQA), no large-scale expert-level dataset has captured stepwise reasoning with precise visual grounding. We introduce S-Chain, the first large-scale dataset of 12,000 expert-annotated medical images with bounding-boxes and structured visual CoT (SV-CoT), explicitly linking visual regions to reasoning steps. The dataset further supports 16 languages, totaling over 700k VQA pairs for broad multilingual applicability. Using S-Chain, we benchmark state-of-the-art medical VLMs (ExGra-Med, LLaVA-Med) and general-purpose VLMs (Qwen2.5-VL, InternVL2.5), showing that SV-CoT supervision significantly improves interpretability, grounding fidelity, and robustness. Beyond benchmarking, we study its synergy with retrieval-augmented generation, revealing how domain knowledge and visual grounding interact during autoregressive reasoning. Finally, we propose a new mechanism that strengthens the alignment between visual evidence and reasoning, improving both reliability and efficiency. S-Chain establishes a new benchmark for grounded medical reasoning and paves the way toward more trustworthy and explainable medical VLMs.

1 Introduction

Large Language Models (LLMs) and Vision Language Models (VLMs) have shown strong capabilities in problem solving, planning, and decision making by learning deductive and inductive reasoning from large-scale data. A key driver is Chain-of-Thought (CoT) reasoning, which breaks complex tasks into step-by-step inferences before reaching a final answer. This paradigm improves performance across domains, from arithmetic and commonsense reasoning in LLM (Wei et al., 2022; Kojima et al., 2022) to Visual Question Answering (VQA) and multimodal reasoning in VLM (Zhang et al., 2023c; Chen et al., 2024a). By externalizing their reasoning process, CoT not only boosts accuracy but also adds interpretability, making them especially promising for high-stakes fields like healthcare.

Despite recent progress, training models with strong CoT reasoning still demands large amounts of annotated data, as models must learn to align intermediate reasoning steps with input evidence (Zelikman et al., 2022; Wang et al., 2022). In general Natural Language Processing (NLP), such supervision can be scaled through crowdsourcing or distillation (Magister et al., 2022; Ho et al., 2023), but in medicine, it is far more costly: annotations must be expert-verified, multimodal, and clinically valid (Moor et al., 2023a; Huang et al., 2024). Beyond this, medical reasoning requires visual grounding, i.e., explicitly linking reasoning steps to Region of Interest (ROI), which adds substantial complexity. As a result, large-scale expert datasets with grounded CoT remain scarce, limiting the training and evaluation of trustworthy medical VLMs.

To mitigate the high cost of expert annotation, recent work has explored auto-generation of CoT data for VLM reasoning. For example, MC-CoT (Wei et al., 2024) leverages modular pipelines where LLMs generate reasoning steps that are loosely aligned with multimodal inputs in zero-shot settings, while MedCoT (Liu et al., 2024) introduces hierarchical expert verification to refine auto-matically produced rationales. Similarly, large medical VQA datasets such as PMC-VQA (Zhang et al., 2023a) rely on template-based or synthetic Question Answering (QA) generation to scale supervision. While such approaches improve data availability, their effectiveness is limited for clinical reasoning due to two key issues: (i) auto-generated CoTs often lack structure, providing free-text explanations without explicit correspondence to specific image regions, which weakens visual ground-

ing; and (ii) they are prone to factual mistakes and hallucinations, frequently introducing redundant or clinically irrelevant content that is difficult to filter out (Gu et al.; Cheng et al., 2025). These limitations highlight the need for high-quality, structured, and expert-grounded CoT annotations in the medical domain.

To address these challenges, we propose a new expert-annotated dataset that provides visually grounded CoTs explicitly linking step-by-step reasoning to visual evidence, which we term Structured Visual Chain-of-Thought (SV-CoT). Our dataset contains 12,000 medical images with bounding-box annotations of ROI, paired with structured rationales that are decomposed into four clinically meaningful stages: (i) object localization, (ii) image captioning, (iii) multiple-choice reasoning, and (iv) image classification. Unlike auto-generated CoTs, each rationale is carefully annotated and verified by medical experts, ensuring both factual accuracy and strong correspondence between reasoning steps and visual features. To enhance accessibility and global applicability, the dataset further supports 16 languages, resulting in over 700,000 QA pairs. By combining structured reasoning, explicit grounding, multilingual coverage, and expert verification, this resource overcomes the key limitations of existing synthetic CoT approaches and establishes a reliable foundation for training and benchmarking medical VLMs.

With this dataset in place, we systematically investigate its impact on the performance of multiple model families, including both domain-specific medical VLMs (e.g., ExGra-Med (Nguyen et al., 2025), LLaVA-Med (Li et al., 2023a)) and general-purpose VLMs (e.g., Qwen2.5-VL (Wang et al., 2024), InternVL2.5 (Chen et al., 2024b)), and compare them against baselines trained with synthetic CoTs generated by GPT-4.1. Beyond standard evaluation, we further assess the integration of our SV-CoT supervision with Retrieval-augmented Generation (RAG) (Zhao et al., 2025; Zheng et al., 2025), examining how external domain-specific knowledge interacts with structured reasoning and visual grounding. A key focus of our analysis is the faithfulness of CoT reasoning and grounding during autoregressive training, where we uncover important discrepancies between textual reasoning steps and the visual evidence they reference. These findings motivate the development of new learning strategies that explicitly reinforce the correlation between grounded visual cues and CoT reasoning, leading to more reliable, interpretable, and clinically trustworthy medical VLMs.

In summary, we make the key contributions as:

- Dataset innovation: We build the first large-scale dataset, Schain, that couples 12k medical images with expert-verified bounding-box annotations and visually grounded reasoning traces, extended to 700k multilingual QA pairs across 16 languages, structured into a four-stage reasoning pipeline to enhance clarity and consistency.
- Extensive evaluation: We conduct a broad comparative study of specialized medical VLMs and general-purpose VLMs, against baselines using GPT-4.1–generated rationales, highlighting the distinctive gains from expert-grounded supervision.
- Analytical insights: We examine how structured visual chain-of-thought reasoning interacts with RAG and probe the faithfulness of CoT alignment with visual grounding during autoregressive training, from which we derive some insights for new learning strategies to tightly couple visual evidence and reasoning.

2 PROBLEM FORMULATION AND KEY CHALLENGES

We study the problem of grounded medical VQA, where the input is a medical image (e.g., a Magnetic Resonance Imaging (MRI) slice) together with a clinically relevant question, and the output is not only a final diagnostic answer but also a SV-CoT that traces the reasoning process back to specific ROIs in the image (Figure 1). In particular, the model has to (i) first identify and localize abnormalities or relevant anatomical structures with bounding boxes, (ii) then provide stepwise reasoning that links visual observations with clinical knowledge, and (iii) finally generate an interpretable answer, such as the disease type or its severity. We term this task SV-CoT, where models must align visual-spatial cues with clinical reasoning to produce interpretable answers. Rather than giving only a final prediction, SV-CoT forces the model to provide stepwise rationales linked to specific image regions, thereby reducing hallucinations and enabling transparent, trustworthy decision-making.

Prior Works. Recent advances in medical VLMs, such as ExGra-Med (Nguyen et al., 2025), LLaVA-Med (Li et al., 2023b), MedGemma (Sellergren et al., 2025), and LLaVA-Tri (Xie et al., 2025).

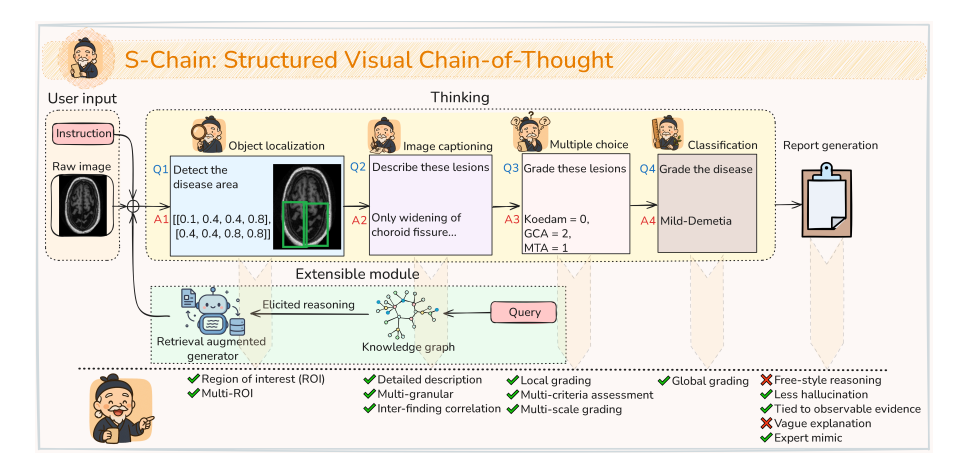


Figure 1: **Overview of the S-Chain dataset with SV-CoT annotations**. Each image is paired with (Q1) ROI localization via bounding boxes, (Q2) lesion descriptions, and (Q3) lesion grading using standardized scales (e.g., Koedam, GCA, MTA). These stepwise annotations ground reasoning in visual evidence, enabling interpretable and reliable medical VQA.

2025), have primarily focused on scaling both model architectures and pre-training corpora to improve accuracy on VQA tasks. These approaches demonstrate that larger model capacity and broader pre-training data can indeed yield stronger overall performance across diverse clinical benchmarks. Yet, despite these gains, such models remain *black boxes* (Borys et al., 2023; AlSaad et al., 2024), producing answers without revealing the clinical reasoning behind them. In practice, valid decisions require systematic analysis of markers (e.g., hippocampal shrinkage, sulcal widening, cortical thinning) and standardized scoring with Scheltens, Pasquier, or Koedam scales. Without reasoning chains that explicitly ground predictions in these features, models cannot provide the transparency essential for trustworthy diagnostic verification.

To enhance interpretability, several recent efforts have explored incorporating CoT reasoning into medical Artificial Intelligence (AI) systems. Datasets such as MedCoT (Liu et al., 2024), MedThink (Gai et al., 2025), ReasonMed (Sun et al., 2025), and the Human-Verified Clinical Reasoning Dataset (HVCR) (Ding et al., 2025) provide additional reasoning traces that improve performance and enable models to output rationales alongside predictions. However, these resources are *restricted to textual CoTs*, without linking reasoning steps to the underlying visual evidence in medical images. Other directions, such as V2T-CoT (Wang et al., 2025), Med-GRIT-270k (Huang et al., 2024), and MedTrinity-25M (Xie et al., 2025), take a step further by pairing reasoning with visual grounding. Yet these datasets are largely generated *using GPT-4.1-based synthetic rationales* built upon existing image—text pairs, which introduces risks of hallucination and factual errors (Figure 4). Such issues are especially concerning in the medical domain, where unreliable grounding boxes or AI-generated explanations and diagnoses may lead to misleading conclusions or inappropriate clinical guidance (Godinho et al., 2010; Shin, 2022; Monfared et al., 2024).

In contrast, **S-Chain** introduces a dataset that directly addresses these limitations by providing expert-validated SV-CoT for 12,000 medical images. Unlike prior synthetic or text-only resources, our dataset ensures faithful alignment between reasoning steps and visual evidence through expert-drawn bounding boxes and clinically verified rationales. Furthermore, with support for 16 languages and over 700,000 high-quality QA pairs, it uniquely combines scale, multilinguality, and expert validation, establishing a diverse foundation for trustworthy, visually grounded reasoning in medical VLMs. Table 1 presents an overall comparison of S-Chain with prior works in the medical domain, while Table 6 (Appendix) extends this comparison to general-domain visual CoT datasets.

3 S-CHAIN DATASET

3.1 STRUCTURED VISUAL CHAIN-OF-THOUGHT DATA

Our dataset targets the task of SV-CoT reasoning for medical VQA. Each example goes beyond the usual image-question-final answer prediction format by following a four-step reasoning (Figure 1) flow that mirrors clinical practice: (Q1) Object localization: bounding boxes highlight ROIs; (Q2) Lesion description: textual explanations describe visible abnormalities (e.g., hippocampal shrinkage, sulcal widening); (Q3) Lesion grading: findings are scored with standardized scales such as Scheltens, Pasquier, or Koedam; and (Q4) Disease classification:

Table 1: Comparison of recent medical reasoning datasets with CoT.

Dataset	Size / Scale	CoT / Reasoning	Visual Ground.	Expert Involve- ment	Multiling.
MedCoT (2024)	Extends Med-VQA (VQA-RAD, SLAKE, PathVQA)	Human-verified CoTs	Х	√ Hierarchical verification	X
MedThink (2025)	Extensions to 3 VQA sets	Decision-making ra- tionales	X	✓ Semi-auto + hu- man pass-through	X
ReasonMed (2025)	370k reasoning sam- ples	Multi-step reasoning paths	X	✓ Multi-agent vali- dation	X
HVCR (2025)	31k QA pairs	Expert-verified CoTs	X	✓	X
V2T-CoT (2025)	~39k examples	GPT-generated CoTs	✓ Partial (region attention)	(No experts)	Х
Med-GRIT-270k (2024)	270k QA pairs	GPT-generated CoTs	✓ Segmentation masks + region refs	(No experts)	×
MedTrinity-25M (2024)	25M ROI-description triplets, 10 modalities	Partial: descriptive text	✓ ROI annotations	✓ Expert validation (~1k subset)	X
S-Chain (Ours, 2025)	12k images / 700k QA pairs	Expert-verified SV-CoTs	✓ Bounding boxes (ROI links)	✓ Full expert an- notation (12k im- ages)	✓ (16 langs.)



Figure 2: **Annotation pipeline**. Experts first select representative 2D slices from MRI volumes (1), then localize ROIs with bounding boxes (2). Abnormalities are described through structured reasoning notes (3) and graded using standardized visual rating scales (4). Annotations undergo expert consensus for quality control (5), and finally, all reasoning steps are translated into several languages with expert validation (6), yielding a multilingual, expert-grounded dataset. (See Appendix Section D.2 for some dataset examples, e.g. Figure 14a).

reasoning steps are predicted into a final diagnostic label (e.g., mild dementia). This structure tightly links visual evidence with reasoning, helping models move from black-box predictions to transparent, clinically grounded decision-making.

3.2 Data Collection

We use the publicly available MRI data from the OASIS: Cross-Sectional Alzheimer's Disease Dataset (Marcus et al., 2007), released under the Apache 2.0 license (see Appendix Section F.1). The dataset contains 3D brain MRI volumes from 461 patients, accompanied by metadata including demographic information and Clinical Dementia Rating (CDR) scores. We collect patients' data that are categorized into three diagnostic groups: Non-Dementia, Mild-Dementia, and Moderate-Dementia, with annotations provided at the volume level.

3.3 DATA ANNOTATION PROCESS

The annotation process was conducted by three trained doctors from different institutions, working independently before consensus review. Since the OASIS dataset provides only volume-level labels, our experts first selected representative 2D slices from each 3D MRI volume to highlight anatomical structures and pathological changes most relevant to Alzheimer's disease (AD)'s progression (e.g., hippocampal shrinkage, ventricular widening). On these slices, ROIs were localized with bounding boxes, described through short reasoning notes, and graded using standardized visual rating scales. Final annotations required consensus among experts to ensure reliability. To broaden accessibility, all QA pairs were extended into 16 languages by certified professional linguists (minimum C1 level) with basic medical training. Figure 2 provides an overview of the pipeline, with stepwise details in Appendix D.1. In total, constructing S-Chain required about **700 hours of expert labor**.

3.4 Data Statistics

Through this process, we curated a dataset of 12,000 expert-annotated medical images with SV-CoT, complemented by 700k QA pairs in 16 languages (English, German, French, Chinese, Japanese,

Arabic, etc). This resource supports the development of medical VLMs that are both multilingual and clinically reliable. As shown in Table 2, the dataset covers 64 patients with non-overlapping train/test splits. Importantly, the test set mirrors real-world dementia cohorts (36% Non-Dementia, 27% Mild, 36% Moderate) as reported in clinical studies (Shin, 2022; Monfared et al., 2024), avoiding the artificially balanced splits common in AI research and ensuring clinically meaningful evaluation.

	#Images				#QA pairs		#Patients			
	Non	Mild	Mod	All	English	All	Non	Mild	Mod	All*
Train Test	4,628 562	4,755 420	1,400 560	,	43,132 6,168	690,112 98,688		27 3	8 5	55 9
S-Chain	5,190	5,175	1,960	12,325	49,300	788,800	27	30	13	64

Table 2: **Statistics of S-Chain dataset**. (*) A patient may show different labels across slices (e.g., Non-Dementia (Non) in one slice, Mild-Dementia (Mild) in another, or Moderate-Dementia (Mod) elsewhere). No overlapping of patients between train and test sets.

3.5 LEARNING SV-COT VIA SUPERVISED FINE-TUNING

To train medical VLMs on SV-CoT, we adopt an **autoregressive Supervised Fine-tuning (SFT)** strategy. Given an input image I and a text prompt corresponding to the final question Q_4 (disease classification), the model is trained to sequentially generate multi-granularity outputs aligned with clinical reasoning steps. Formally, the model learns a distribution:

$$P(Y \mid I, Q_4) = \prod_{t=1}^{T} P(y_t \mid I, Q_4, y_{< t}), \tag{1}$$

where the output sequence $Y=(Y_1,Y_2,Y_3,Y_4)$ corresponds to the structured reasoning stages: $Y_1=$ bounding box coordinates of ROIs (textual form), $Y_2=$ lesion descriptions grounded in these regions, $Y_3=$ lesion grading using standardized scales, and $Y_4=$ the final diagnostic label. Note that the procedural questions (i.e., Q_1,Q_2 , and Q_3) are embedded in the corresponding output sequences (i.e., Y_1,Y_2 , and Y_3 , respectively). Training is performed with teacher-forced **cross-entropy loss** against expert-annotated sequences:

$$\mathcal{L}_{\text{SV-CoT}} = -\sum_{t=1}^{T} \log P(y_t^* \mid I, Q_4, y_{< t}^*), \tag{2}$$

where y_t^* denotes the expert-verified token at step t. This formulation enforces the model to generate **intermediate reasoning traces** (localization, description, grading) before arriving at the clinically meaningful answer, thereby improving interpretability and grounding.

4 S-CHAIN IN ACTION: EXPERIMENTAL VALIDATION

In this section, we conduct three groups of experiments to assess the impact of the S-Chain dataset on medical reasoning with VLMs. Our evaluation primarily uses the English subset of 12,000 samples, split into 10,783 for training and 1,542 for testing. In which:

Baselines. We evaluate three groups of baselines: (i) Medical-domain VLMs: ExGra-Med (7B) (Nguyen et al., 2025), LLaVA-Med (7B) (Li et al., 2023b), MedGemma (4B) (Sellergren et al., 2025), and MedFlamingo (7B) (Moor et al., 2023b). These models represent state-of-the-art architectures adapted for clinical applications; ii) General-purpose VLMs: Qwen2.5-VL (Yang et al., 2024) and InternVL2.5 (Chen et al., 2024b). Both serve as strong open-source baselines outside the medical domain; (iii) Closed-source API models (zero-/few-shot settings): We use GPT-4.1 (OpenAI, 2025a), GPT-o3 (OpenAI, 2025b), Grok-4 (xAI, 2025), and Gemini-2.5-Flash (DeepMind, 2025).

All fine-tunable models are trained on the S-Chain dataset with the SFT procedure described in Section 3.5, while API models are directly evaluated through in-context reasoning under zero-shot, 4-shot, 8-shot, and 16-shot prompting settings, where representative input—output examples are included in the system prompt (see Figure 7 and Figure 8 in Appendix Section A.2 for system prompts).

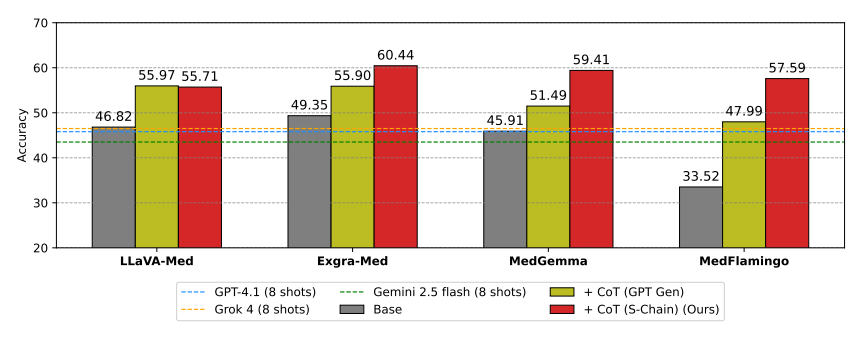


Figure 3: Accuracy of medical VLMs trained with the **base setting** (Q4-only), **synthetic GPT-4.1 CoTs**, and expert-annotated **S-Chain SV-CoTs** (ours). S-Chain consistently improves performance across models, with closed-source APIs (GPT-4.1, Grok-4, Gemini-2.5-Flash) shown for 8-shot reference.

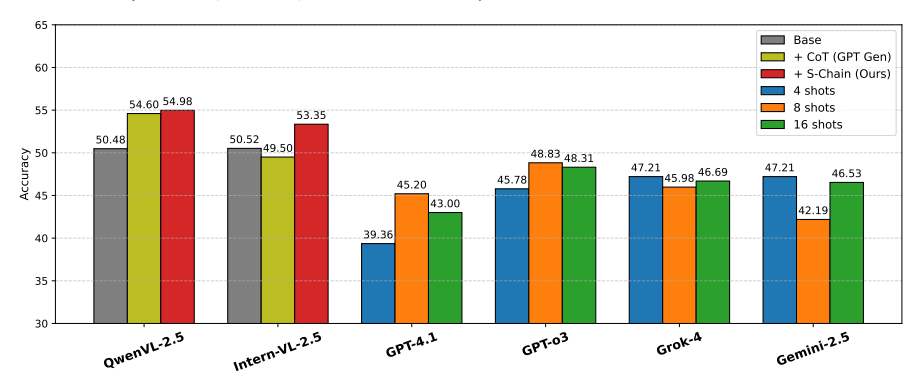


Figure 4: Accuracy of general-purpose VLMs trained with the **base setting** (Q4-only), **synthetic GPT-4.1 CoTs**, and expert-annotated **S-Chain SV-CoTs** (ours). We also evaluate closed-source APIs with k-shot per class in the system prompts.

Task and Metrics: We evaluate models primarily on disease classification (Q4), reporting both *Accuracy* and *F1* to capture overall correctness and class balance. Intermediate steps are also assessed: bounding box localization (Q1) with *mIoU*, lesion grading (Q3) with Accuracy against expert scores, and CoT descriptions (Q2) with *BLEU*, *METEOR*, *BERTScore* for semantic similarity for faithfulness and clinical plausibility.

4.1 S-CHAIN VS. SYNTHETIC GROUNDING: THE VALUE OF EXPERT ANNOTATIONS We evaluate both medical-domain and general-purpose VLMs using the S-Chain dataset under three training setups:

- (i) Base setting (Q4-only): models are trained to predict only the final diagnostic answer, without any reasoning supervision. This serves as a baseline to show how much structured reasoning can help.
- (ii) S-Chain supervision: models are trained with our expert-annotated SV-CoT data, which includes intermediate steps such as ROI localization, lesion description, grading, and final classification.
- (iii) **Synthetic CoT supervision**: models are trained with CoTs generated by GPT-4.1. Here, the model is prompted with the image, question, and ground-truth answer, and asked to produce bounding boxes and rationales (see Figure 9 in Appendix Section A.2 for system prompts).

This comparison aims to highlight the added value of expert-level annotations in S-Chain, and contrasts them with GPT-generated CoTs commonly used in prior work.

Our results in Figure 3 show that S-Chain supervision consistently outperforms both the Q4-only baseline (10-15%) and GPT-4.1–generated synthetic CoTs (4-5%), underscoring the necessity of expert-verified annotations for trustworthy reasoning. Complementing this, Table 3 reports intermediate-step performance on representative models (ExGra-Med and MedGemma), covering ROI localization and CoT quality. Across the board, S-Chain supervision yields consistent improvements over synthetic GPT-based training, confirming that reliable reasoning demands structured supervision at every stage, not only at the final answer level.

Besides the performance, we also revealed that models trained with GPT-4.1 synthetic CoTs often inherit hallucinations from the teacher model, yielding incomplete or inconsistent reasoning traces. As illustrated in Figure 4, GPT-generated ROIs frequently **exhibit missing, misaligned**, or **absent bounding boxes** (Figure 10 Appendix), undermining the grounding of reasoning. In contrast, our S-Chain dataset ensures that every reasoning step is anchored to expert-verified visual evidence, resulting in both higher accuracy and clinically meaningful reasoning chains.

Beyond medical-domain VLMs, we show that S-Chain also provides measurable benefits to general-purpose VLMs such as Qwen2.5-VL and InternVL2.5 (Figure 4). Furthermore, when benchmarking closed-source API models (GPT-4.1, GPT-o3, Grok-4, Gemini-2.5-Flash), we prompt them with few-shot exemplars per disease class using $k \in \{4, 8, 16\}$. Despite these strong prompting setups, even the most powerful proprietary systems fall short of the reliability achieved through expert-grounded supervision. Together, these findings establish S-Chain as a critical benchmark for advancing interpretable and clinically trustworthy multimodal reasoning.

Table 3: Evaluation of intermediate reasoning steps on ExGra-Med and LLaVA-Med using our S-Chain and GPT-synthetic CoT data. Q1 is bounding-box localization (mIoU). Q2 is CoT text quality measured by BLEU, METEOR, and BERTScore (F1). Best results per row are in **bold**. We observe a consistent enhanced accuracy across models when trained by S-Chain against GPT4-synthetic CoT.

Model	Training Data	mIoU	BLEU	METEOR	BERTScore (F1)
ExGra-Med	GPT-Syn. CoT	4.3	17.9	37.8	73.7
	S-Chain (Ours)	25.3	28.4	42.4	77.7
LLaVA-Med	GPT-Syn. CoT	4.2	17.9	38.2	73.6
	S-Chain (Ours)	23.3	27.3	41.1	77.4

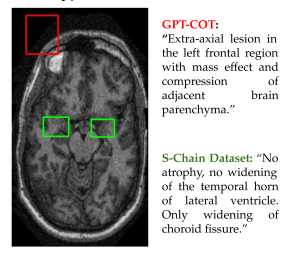


Table 4: **Qualitative results.** GPT-generated CoTs might predict false or misplaced bounding boxes (red) and introduce hallucinated lesion descriptions that are not supported by the image in the green boxes. See Figure 10 in Appendix Section C.1 for more qualitative results.

4.2 SYNERGY OF EXTERNAL MEDICAL KNOWLEDGE AND S-CHAIN

In this section, we investigate whether incorporating **external medical knowledge** through RAG (**MedRAG**) can further enhance reasoning when combined with our SV-CoT supervision. The key idea is that SV-CoT provides faithful, stepwise alignment between visual evidence and reasoning, while MedRAG can supply complementary domain knowledge that may be missing from image-based cues alone.

To evaluate this, we consider three experimental settings: (i) **Base + MedRAG**: the model receives retrieved medical passages as additional context but is trained without SV-CoT supervision; (ii) **Base + SV-CoT**: the model is trained with expert-grounded reasoning steps but with

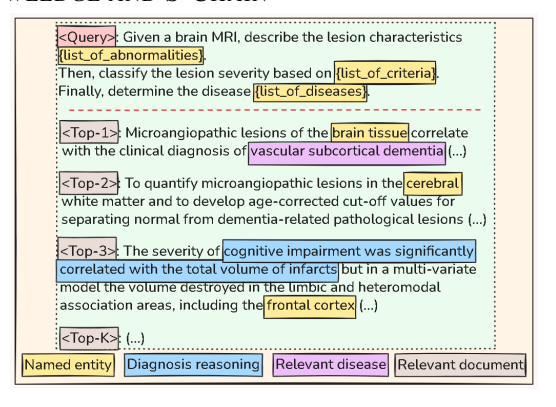


Figure 5: A query to MIRIAD for the retrieval of the top relevant descriptions.

out external retrieval; (iii) **Base + SV-CoT + MedRAG**: both structured reasoning and external knowledge are combined to support the decision process.

4.2.1 Retrieval Protocol. To provide high-quality external knowledge for our models, we adopt the MIRIAD framework - a large, curated corpus of medical instruction-response pairs grounded in peer-reviewed literature (Zheng et al., 2025). MIRIAD is designed to support RAG in healthcare, reducing the noise of generic web text and ensuring medically reliable content.

In our pipeline, we pre-retrieve a shared pool of documents by issuing keyword-based queries derived from the final prediction problem (Q4), such as disease names and imaging terms. The top-k retrieved instruction-response passages (typically k=5) are then associated with all questions linked to that prediction task (Figure 5). During training and inference, these passages are concatenated into the input context alongside the image and question, providing the model with additional

factual background. This protocol ensures that retrieval is both task-targeted (anchored in Q4 disease classification) and consistent across related questions, allowing us to isolate the effect of combining SV-CoT supervision with medically grounded external knowledge.

4.2.2 Observations. Table 5 demonstrates that MedRAG provides consistent but modest improvements over the base models across both medical and general-purpose VLMs, with gains typically in the range of 1-5% Accuracy. In contrast, SV-CoT supervision yields far larger benefits, boosting performance by up to +13.5 Accuracy and +14.6 F1 on MedGemma. When the two approaches are combined (SV-CoT + MedRAG), models mostly achieve their strongest results, with improvements as high as +15.4 Accuracy and +15.7 F1 on ExGra-Med. These findings suggest that while RAG contributes useful complementary knowledge, expert-grounded reasoning (SV-CoT) is the dominant driver of performance, and the synergy of the two offers the most reliable path toward clinically trustworthy reasoning.

Table 5: Impact of MedRAG and SV-CoT on Q4 performance. Scores are Accuracy / F1. Δ is absolute Accuracy gain over Base. Best and second per row in **bold** and underline.

Model	Base	+ MedRAG		+ SV-CoT		+ SV-CoT + MedRAG	
	(Acc / F1)	Score	Δ	Score	Δ	Score	Δ
ExGra-Med	49.4 / 46.9	50.3 / 48.7	+0.9/+1.8	60.4 / 59.6	+11/+12.7	64.8 /62.6	+15.4/+15.7
LLaVA-Med	46.8 / 43.2	50.8/48.9	+4/+5.7	55.7 / 53.0	+8.9/+9.8	59.5 / 57.8	+12.7/+14.6
MedGemma	45.9 / 42.1	47.6 / 44.4	+1.7/+2.3	59.4 / 56.7	+13.5/+14.6	56.7 / 52.9	+10.8/+10.8
Qwen2.5-VL	50.5 / 45.6	54.3 / 54.2	+3.8/+8.6	55.0 / 49.4	+4.5/+3.8	60.8 / 47.9	+10.3 / 2.3
InternVL2.5	50.5 / 47.6	52.3 / 43.3	+1.8/-4.3	$\overline{53.4} / \overline{48.8}$	+2.9/1.2	58.3 / 54.6	+7.8/+7

4.3 FAITHFULNESS OF COT REASONING AND VISUAL GROUNDING

A central challenge in multimodal reasoning is ensuring that generated CoTs are faithful to the visual evidence they claim to describe. In medical VQA, this faithfulness means that the reasoning process must explicitly incorporate the ROIs localized in Q1, rather than producing generic or hallucinated explanations disconnected from the image. Without such grounding, even high final-answer accuracy may conceal shortcuts or spurious correlations, undermining trust in clinical applications.

To probe this issue, we analyze ExGra-Med, a state-of-the-art model, and test whether its grounded CoTs truly reflect bounding-box information. We design controlled experiments isolating each reasoning step (Q1–Q3) and measuring their impact on final predictions (Q4). This setup evaluates both overall performance and how well CoTs align with visual evidence, offering a principled way to assess and improve faithfulness in medical VLMs.

A. Component-wise Evaluation of Reasoning Steps. We run controlled experiments on the S-Chain dataset (Figure 6) under four settings: (i) standard SFT with no extra inputs at inference; (ii) the same, but with ground-truth ROIs (Q1) provided; (iii) ground-truth ROIs and CoTs (Q1–Q2) given; and (iv) all ground-truth intermediate steps (Q1–Q3) supplied, leaving only Q4 to predict.

Results reveal a clear trend: providing ground-truth ROIs in (ii) yields modest gains in Q4 accuracy (\sim 2%), while supplying correct CoTs in (iii) nearly solves the task, pushing accuracy to 99%. This highlights a key insight: when CoTs are accurate and faithful, the final diagnostic task (Q4) becomes almost trivial. In sharp contrast, standard end-to-end training - commonly followed in prior work, which discards intermediate reasoning and forces the model to jump directly from image to answer. This not only increases task difficulty but also undermines interpretability and reliability, underscoring the need for structured supervision as a foundation for trustworthy medical VLMs.

B. Bounding Boxes and Grounded CoT Correlation. Given our finding that accurate CoT generation is the decisive factor for Q4 reliability, we next examine how ROI representation influences reasoning. Since CoTs are generated auto-regressively conditioned on localized regions, the form of ROI input plays a critical role in aligning reasoning with visual evidence. We compare two strategies: (i) textual supervision, where bounding box coordinates are appended to the training text, and (ii) **visual prompting**, where ROIs are explicitly highlighted on the image. For (i), we additionally test whether perturbing the ROI text, or removing ROI information entirely, affects the quality of CoT outputs (see Appendix, Section B).

Controlled evaluations with ground-truth ROIs (Figure 6) show a clear contrast. Under textual supervision, models often reference anatomical terms but weakly attend to numeric box coordinates,

leading to hallucinated or incomplete CoTs (0.62 Acc). By contrast, visual prompting yields CoTs that consistently reference the true localized abnormalities and avoid irrelevant details (0.73 Acc). This shows that anchoring attention to ROIs strengthens evidence–reasoning alignment, yielding more clinically faithful CoTs.

C. Toward Faithful Vision-Language Reasoning. Building on our component-wise and ROI-CoT analyses, we propose a lightweight regularization to improve reasoning faithfulness. In contrast to standard auto-regressive generation, we explicitly link CoT embeddings to visual tokens: they are encouraged to align with ROI tokens while being repelled from non-ROIs. To further enhance discriminability, CoT embeddings from different disease categories are also regularized to remain separated, promoting reasoning patterns that are both grounded and clinically distinct.

In particular, let I be an image tokenized into vision embeddings $\mathcal{V} = \{v_i\}_{i=1}^M$, with an ROI index set $\mathcal{R} \subset \{1,\ldots,M\}$ and its complement $\bar{\mathcal{R}}$. Given the question Q_4 and the model's grounded CoT sequence (Q_2 outputs) $Y_{\text{CoT}} = (y_1,\ldots,y_T)$, let $c \in \mathbb{R}^d$ denote a mean CoT embedding, i.e., the mean-pooled hidden state of CoT tokens. Besides training with the SFT as Equation 2, we further add two regularizers:

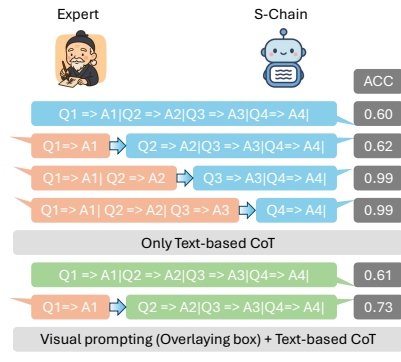


Figure 6: Control experiments evaluating the role of each SV-CoT component. Light peach blocks show ground-truth inputs at test time, while blue/green blocks are model-generated. Upper settings use text-based CoTs, and lower settings use visual prompting to ground reasoning in ROIs.

(i) ROI anchoring (CoT \leftrightarrow vision tokens). We encourage c to align with ROI tokens and be repelled from non-ROI tokens via an margin-based InfoNCE-style loss (define m>0 as the margin):

$$\mathcal{L}_{\text{margin}} = \max \left(0, m + \frac{1}{|\bar{\mathcal{R}}|} \sum_{j \in \bar{\mathcal{R}}} \cos(c, v_j) - \frac{1}{|\mathcal{R}|} \sum_{i \in \mathcal{R}} \cos(c, v_i) \right), \tag{3}$$

(ii) Inter-disease separation (CoT \leftrightarrow CoT). For a batch \mathcal{B} of samples with CoT embeddings $\{c_b\}$ and disease labels $\{y_b\}$, we use a supervised contrastive loss to push apart CoTs from different diseases and pull together those from the same disease:

$$\mathcal{L}_{\text{SupCon}} = -\sum_{a \in \mathcal{B}} \frac{1}{|P(a)|} \sum_{p \in P(a)} \log \frac{\exp(\langle c_a, c_p \rangle / \tau_d)}{\sum_{b \in \mathcal{B} \setminus \{a\}} \exp(\langle c_a, c_b \rangle / \tau_d)},\tag{4}$$

where $P(a) = \{ p \in \mathcal{B} : y_p = y_a, p \neq a \}$. With additional SFT under the proposed conditions, ExGra-Med improves from 60.4% to 62.5% in Accuracy and from 59.6% to 61.7% in F1. Although modest, these gains highlight that stronger alignment between CoT reasoning and ROI localization is a promising direction. Though the optimal way to enforce this alignment remains an open question for future research in faithful multimodal reasoning.

4.4 DISCUSSIONS

Our study demonstrates that SV-CoTs provides clear benefits for medical reasoning, yielding measurable improvements over both Q4-only baselines and GPT-synthetic CoTs. By explicitly linking reasoning steps to visual ROIs, SV-CoTs not only enhances predictive accuracy but also improves interpretability and reduces hallucinations. Combining SV-CoTs with MedRAG brings further gains, underscoring the complementary roles of grounded reasoning and external knowledge. Nonetheless, *current S-Chain datasets remain limited in diagnostic coverage*, exhibit overly linear reasoning compared to real clinical workflows, and lack temporal or multi-expert dynamics. Addressing these gaps will be important to test SV-CoTs in broader and more realistic settings.

Looking ahead, ensuring faithful CoT generation remains an open challenge. Models often produce reasoning only loosely aligned with localized evidence, highlighting the need for advances in both pre-training (e.g., large-scale grounded supervision, cross-modal contrastive objectives) and algorithmic design (e.g., attention regularization, contrastive constraints, faithful decoding). Progress along these directions will be crucial to develop VLMs that are not only accurate but also clinically trustworthy, bridging the gap between black-box predictions and transparent decision-making.

REFERENCES

- Omar M Al-Janabi, Pradeep Panuganti, Erin L Abner, Ahmed A Bahrani, Ronan Murphy, Shoshana H Bardach, Allison Caban-Holt, Peter T Nelson, Brian T Gold, Charles D Smith, et al. Global cerebral atrophy detected by routine imaging: relationship with age, hippocampal atrophy, and white matter hyperintensities. *Journal of Neuroimaging*, 28(3):301–306, 2018.
- Ricardo Francisco Allegri. Moving from neurodegenerative dementias, to cognitive proteinopathies, replacing "where" by "what".... *Dementia & neuropsychologia*, 14:237–242, 2020.
- Rawan AlSaad, Alaa Abd-Alrazaq, Sabri Boughorbel, Arfan Ahmed, Max-Antoine Renault, Rafat Damseh, and Javaid Sheikh. Multimodal large language models in health care: applications, challenges, and future outlook. *Journal of medical Internet research*, 26:e59505, 2024.
- Liana G Apostolova. Alzheimer disease. Continuum: Lifelong Learning in Neurology, 22(2):419–434, 2016.
- Ingrid Arevalo-Rodriguez, Nadja Smailagic, Marta Roqué i Figuls, Agustín Ciapponi, Erick Sanchez-Perez, Antri Giannakou, Olga L Pedraza, Xavier Bonfill Cosp, and Sarah Cullum. Minimental state examination (mmse) for the detection of alzheimer's disease and other dementias in people with mild cognitive impairment (mci). *Cochrane database of systematic reviews*, (3), 2015.
- Lynn M Bekris, Chang-En Yu, Thomas D Bird, and Debby W Tsuang. Genetics of alzheimer disease. *Journal of geriatric psychiatry and neurology*, 23(4):213–227, 2010.
- Matthew Bobinski, MJ De Leon, J Wegiel, S Desanti, A Convit, LA Saint Louis, H Rusinek, and HM Wisniewski. The histological validation of post mortem magnetic resonance imaging-determined hippocampal volume in alzheimer's disease. *Neuroscience*, 95(3):721–725, 1999.
- Katarzyna Borys, Yasmin Alyssa Schmitt, Meike Nauta, Christin Seifert, Nicole Krämer, Christoph M Friedrich, and Felix Nensa. Explainable ai in medical imaging: An overview for clinical practitioners—beyond saliency-based xai approaches. *European journal of radiology*, 162: 110786, 2023.
- Heiko Braak and Eva Braak. Neuropathological stageing of alzheimer-related changes. *Acta neuropathologica*, 82(4):239–259, 1991.
- Benjamin H Brinkmann, Hari Guragain, Daniel Kenney-Jung, Jay Mandrekar, Robert E Watson, Kirk M Welker, Jeffrey W Britton, and Robert J Witte. Segmentation errors and intertest reliability in automated and manually traced hippocampal volumes. *Annals of clinical and translational neurology*, 6(9):1807–1814, 2019.
- Marie Bruun, Hanneke FM Rhodius-Meester, Juha Koikkalainen, Marta Baroni, Le Gjerum, Afina W Lemstra, Frederik Barkhof, Anne M Remes, Timo Urhemaa, Antti Tolonen, et al. Evaluating combinations of diagnostic tests to discriminate different dementia types. *Alzheimer's & Dementia: Diagnosis, Assessment & Disease Monitoring*, 10:509–518, 2018.
- Jesse M Cedarbaum, Mark Jaros, Chito Hernandez, Nicola Coley, Sandrine Andrieu, Michael Grundman, Bruno Vellas, Alzheimer's Disease Neuroimaging Initiative, et al. Rationale for use of the clinical dementia rating sum of boxes as a primary outcome measure for alzheimer's disease clinical trials. *Alzheimer's & Dementia*, 9(1):S45–S55, 2013.
- Michael A Chappell, Flora A Kennedy McConnell, Xavier Golay, Matthias Günther, Juan A Hernandez-Tamames, Matthias J van Osch, and Iris Asllani. Partial volume correction in arterial spin labeling perfusion mri: A method to disentangle anatomy from physiology or an analysis step too far? *Neuroimage*, 238:118236, 2021.
- Qiguang Chen, Libo Qin, Jin Zhang, Zhi Chen, Xiao Xu, and Wanxiang Che. M³ cot: A novel benchmark for multi-domain multi-step multi-modal chain-of-thought. *arXiv preprint arXiv:2405.16473*, 2024a.

- Zhe Chen, Jiannan Wu, Wenhai Wang, Weijie Su, Guo Chen, Sen Xing, Muyan Zhong, Qinglong Zhang, Xizhou Zhu, Lewei Lu, et al. Internvl: Scaling up vision foundation models and aligning for generic visual-linguistic tasks. In *Proceedings of the IEEE/CVF conference on computer vision and pattern recognition*, pp. 24185–24198, 2024b.
 - Zihui Cheng, Qiguang Chen, Jin Zhang, Hao Fei, Xiaocheng Feng, Wanxiang Che, Min Li, and Libo Qin. Comt: A novel benchmark for chain of multi-modal thought on large vision-language models. In *Proceedings of the AAAI Conference on Artificial Intelligence*, volume 39, pp. 23678–23686, 2025.
 - Leonidas Chouliaras and John T O'Brien. The use of neuroimaging techniques in the early and differential diagnosis of dementia. *Molecular Psychiatry*, 28(10):4084–4097, 2023.
 - Rosa M Crum, James C Anthony, Susan S Bassett, and Marshal F Folstein. Population-based norms for the mini-mental state examination by age and educational level. *Jama*, 269(18):2386–2391, 1993.
 - Google DeepMind. Gemini model thinking updates march 2025. https://blog.google/technology/google-deepmind/gemini-model-thinking-updates-march-2025/?utm_source=chatgpt.com, March 2025. Accessed: 2025-09-23.
 - Chao Ding, Mouxiao Bian, Pengcheng Chen, Hongliang Zhang, Tianbin Li, Lihao Liu, Jiayuan Chen, Zhuoran Li, Yabei Zhong, Yongqi Liu, et al. Building a human-verified clinical reasoning dataset via a human llm hybrid pipeline for trustworthy medical ai. *arXiv preprint arXiv:2505.06912*, 2025.
 - George A Edwards III, Nazaret Gamez, Gabriel Escobedo Jr, Olivia Calderon, and Ines Moreno-Gonzalez. Modifiable risk factors for alzheimer's disease. *Frontiers in aging neuroscience*, 11: 146, 2019.
 - Daniel Ferreira, Lena Cavallin, E-M Larsson, J-S Muehlboeck, Patrizia Mecocci, Bruno Vellas, Magda Tsolaki, Iwona Kłoszewska, Hilkka Soininen, Simon Lovestone, et al. Practical cut-offs for visual rating scales of medial temporal, frontal and posterior atrophy in a lzheimer's disease and mild cognitive impairment. *Journal of internal medicine*, 278(3):277–290, 2015.
 - Giorgio G Fumagalli, Paola Basilico, Andrea Arighi, Matteo Mercurio, Marta Scarioni, Tiziana Carandini, Annalisa Colombi, Anna M Pietroboni, Luca Sacchi, Giorgio Conte, et al. Parieto-occipital sulcus widening differentiates posterior cortical atrophy from typical alzheimer disease. *NeuroImage: Clinical*, 28:102453, 2020.
 - Xiaotang Gai, Chenyi Zhou, Jiaxiang Liu, Yang Feng, Jian Wu, and Zuozhu Liu. Medthink: A rationale-guided framework for explaining medical visual question answering. In *Findings of the Association for Computational Linguistics: NAACL 2025*, pp. 7438–7450, 2025.
 - Cláudia Godinho, Iulek Gorczevski, Andréa Heisler, Maria Otília Cerveira, and Márcia Lorena Chaves. Clinical and demographic characteristics of elderly patients with dementia assisted at an outpatient clinic in southern brazil. *Dementia & Neuropsychologia*, 4(1):42–46, 2010.
 - Jonathan Graff-Radford, Keir XX Yong, Liana G Apostolova, Femke H Bouwman, Maria Carrillo, Bradford C Dickerson, Gil D Rabinovici, Jonathan M Schott, David T Jones, and Melissa E Murray. New insights into atypical alzheimer's disease in the era of biomarkers. *The Lancet Neurology*, 20(3):222–234, 2021.
 - Zishan Gu, Jiayuan Chen, Fenglin Liu, Changchang Yin, and Ping Zhang. Medvh: Toward systematic evaluation of hallucination for large vision language models in the medical context. *Advanced Intelligent Systems*, pp. 2500255.
 - Harald Hampel, Jeffrey Cummings, Kaj Blennow, Peng Gao, Clifford R Jack Jr, and Andrea Vergallo. Developing the atx (n) classification for use across the alzheimer disease continuum. *Nature Reviews Neurology*, 17(9):580–589, 2021.

- Lorna Harper, Frederik Barkhof, Nick C Fox, and Jonathan M Schott. Using visual rating to diagnose dementia: a critical evaluation of mri atrophy scales. *Journal of Neurology, Neurosurgery & Psychiatry*, 86(11):1225–1233, 2015.
 - Yunlin He, Xingxing Zhu, Kaixuan Wang, Jikui Xie, Zehua Zhu, Ming Ni, Shicun Wang, and Qiang Xie. Design, synthesis, and preliminary evaluation of [18f]-aryl flurosulfates pet radiotracers via sufex methods for β -amyloid plaques in alzheimer's disease. *Bioorganic & Medicinal Chemistry*, 75:117087, 2022.
 - Namgyu Ho, Laura Schmid, and Se-Young Yun. Large language models are reasoning teachers. *arXiv preprint arXiv:2212.10071*, 2023.
 - Xiaoshuang Huang, Haifeng Huang, Lingdong Shen, Yehui Yang, Fangxin Shang, Junwei Liu, and Jia Liu. A refer-and-ground multimodal large language model for biomedicine. In *International Conference on Medical Image Computing and Computer-Assisted Intervention*, pp. 399–409. Springer, 2024.
 - Clifford R Jack Jr, David A Bennett, Kaj Blennow, Maria C Carrillo, Billy Dunn, Samantha Budd Haeberlein, David M Holtzman, William Jagust, Frank Jessen, Jason Karlawish, et al. Nia-aa research framework: toward a biological definition of alzheimer's disease. *Alzheimer's & dementia*, 14(4):535–562, 2018.
 - Young Jin Jeong, Hyoung Suk Park, Ji Eun Jeong, Hyun Jin Yoon, Kiwan Jeon, Kook Cho, and Do-Young Kang. Restoration of amyloid pet images obtained with short-time data using a generative adversarial networks framework. *Scientific reports*, 11(1):4825, 2021.
 - Dongzhi Jiang, Renrui Zhang, Ziyu Guo, Yanwei Li, Yu Qi, Xinyan Chen, Liuhui Wang, Jianhan Jin, Claire Guo, Shen Yan, et al. Mme-cot: Benchmarking chain-of-thought in large multimodal models for reasoning quality, robustness, and efficiency. In *Forty-second International Conference on Machine Learning*, 2025.
 - Celeste M Karch and Alison M Goate. Alzheimer's disease risk genes and mechanisms of disease pathogenesis. *Biological psychiatry*, 77(1):43–51, 2015.
 - Surabhi Kaushik, Kavita Vani, Shishir Chumber, Kuljeet Singh Anand, and Rajinder K Dhamija. Evaluation of mr visual rating scales in major forms of dementia. *Journal of Neurosciences in Rural Practice*, 12(1):16, 2020.
 - Esther LGE Koedam, Manja Lehmann, Wiesje M van der Flier, Philip Scheltens, Yolande AL Pijnenburg, Nick Fox, Frederik Barkhof, and Mike P Wattjes. Visual assessment of posterior atrophy development of a mri rating scale. *European radiology*, 21(12):2618–2625, 2011.
 - Takeshi Kojima, Shixiang Shane Gu, Machel Reid, Yutaka Matsuo, and Yusuke Iwasawa. Large language models are zero-shot reasoners. *Advances in neural information processing systems*, 35:22199–22213, 2022.
 - Anil Kumar, Jaskirat Sidhu, Forshing Lui, and Jack W Tsao. Alzheimer disease. In *StatPearls [internet]*. StatPearls Publishing, 2024a.
 - Anil Kumar, Jaskirat Sidhu, Forshing Lui, and Jack W Tsao. Alzheimer disease. In *StatPearls [internet]*. StatPearls Publishing, 2024b.
 - Chunyuan Li, Cliff Wong, Sheng Zhang, Naoto Usuyama, Haotian Liu, Jianwei Yang, Tristan Naumann, Hoifung Poon, and Jianfeng Gao. Llava-med: Training a large language-and-vision assistant for biomedicine in one day. *Advances in Neural Information Processing Systems*, 36: 28541–28564, 2023a.
- Chunyuan Li, Cliff Wong, Sheng Zhang, Naoto Usuyama, Haotian Liu, Jianwei Yang, Tristan Naumann, Hoifung Poon, and Jianfeng Gao. Llava-med: Training a large language-and-vision assistant for biomedicine in one day. *Advances in Neural Information Processing Systems*, 36: 28541–28564, 2023b.

- Yueran Li, Huifang Xu, Huifang Wang, Kui Yang, Jiajie Luan, and Sheng Wang. Trem2: Potential therapeutic targeting of microglia for alzheimer's disease. *Biomedicine & Pharmacotherapy*, 165: 115218, 2023c.
 - Jiaxiang Liu, Yuan Wang, Jiawei Du, Joey Tianyi Zhou, and Zuozhu Liu. Medcot: Medical chain of thought via hierarchical expert. *Proceedings of the 2024 Conference on Empirical Methods in Natural Language Processing*, 2024.
 - EJA Loewenstein, TG Maria, A Amarilis, S Elizabeth, B Warren, WH Yougui, et al. Volumetic and visual rating of mri scans in the diagnosis of amnestic mci and alzheimer's disease. *Alzheimer Dement*, 7:1–17, 2011.
 - Zhuqing Long, Jie Li, Jianghua Fan, Bo Li, Yukeng Du, Shuang Qiu, Jichang Miao, Jian Chen, Juanwu Yin, and Bin Jing. Identifying alzheimer's disease and mild cognitive impairment with atlas-based multi-modal metrics. *Frontiers in Aging Neuroscience*, 15:1212275, 2023.
 - Pan Lu, Swaroop Mishra, Tanglin Xia, Liang Qiu, Kai-Wei Chang, Song-Chun Zhu, Oyvind Tafjord, Peter Clark, and Ashwin Kalyan. Learn to explain: Multimodal reasoning via thought chains for science question answering. Advances in Neural Information Processing Systems, 35:2507–2521, 2022.
 - CA Lynch, C Walsh, A Blanco, M Moran, RF Coen, JB Walsh, and BA Lawlor. The clinical dementia rating sum of box score in mild dementia. *Dementia and geriatric cognitive disorders*, 21(1):40–43, 2005.
 - Lucie Charlotte Magister, Jonathan Mallinson, Jakub Adamek, Eric Malmi, and Aliaksei Severyn. Teaching small language models to reason. *arXiv preprint arXiv:2212.08410*, 2022.
 - Daniel S Marcus, Tracy H Wang, Jamie Parker, John G Csernansky, John C Morris, and Randy L Buckner. Open access series of imaging studies (oasis): cross-sectional mri data in young, middle aged, nondemented, and demented older adults. *Journal of cognitive neuroscience*, 19(9):1498–1507, 2007.
 - Gustav Mårtensson, Claes Håkansson, Joana B Pereira, Sebastian Palmqvist, Oskar Hansson, Danielle van Westen, and Eric Westman. Medial temporal atrophy in preclinical dementia: visual and automated assessment during six year follow-up. *NeuroImage: Clinical*, 27:102310, 2020.
 - Guy M McKhann, David S Knopman, Howard Chertkow, Bradley T Hyman, Clifford R Jack Jr, Claudia H Kawas, William E Klunk, Walter J Koroshetz, Jennifer J Manly, Richard Mayeux, et al. The diagnosis of dementia due to alzheimer's disease: recommendations from the national institute on aging-alzheimer's association workgroups on diagnostic guidelines for alzheimer's disease. *Alzheimer's & dementia*, 7(3):263–269, 2011.
 - Jifei Miao, Haixia Ma, Yang Yang, Yuanpin Liao, Cui Lin, Juanxia Zheng, Muli Yu, and Jiao Lan. Microglia in alzheimer's disease: Pathogenesis, mechanisms, and therapeutic potentials. Frontiers in aging neuroscience, 15:1201982, 2023.
 - Anna Molinder, Doerthe Ziegelitz, Stephan E Maier, and Carl Eckerström. Validity and reliability of the medial temporal lobe atrophy scale in a memory clinic population. *BMC neurology*, 21: 1–10, 2021.
 - Amir Abbas Tahami Monfared, N Hummel, A Chandak, A Khachatryan, R Zhang, and Q Zhang. Prevalence estimation of dementia/alzheimer's disease using health and retirement study database in the united states. *The Journal of Prevention of Alzheimer's Disease*, 11(5):1183–1188, 2024.
 - M Monica Moore, Mirella Díaz-Santos, and Keith Vossel. Alzheimer's association 2021 facts and figures report. *Alzheimer's Association*, 17(3):327–406, 2021.
 - Stefany Montufar, Cristian Calero, Rodrigo Vinueza, Patricio Correa, Andrea Carrera-Gonzalez, Franklin Villegas, Germania Moreta, and Rosario Paredes. Association between the apoe $\varepsilon 4$ allele and late-onset alzheimer's disease in an ecuadorian mestizo population. *International Journal of Alzheimer's Disease*, 2017(1):1059678, 2017.

- Michael Moor, Osbert Banerjee, Zeming Abad, and et al. Foundation models for generalist medical artificial intelligence. *Nature*, 616(7956):259–265, 2023a.
 - Michael Moor, Qian Huang, Shirley Wu, Michihiro Yasunaga, Yash Dalmia, Jure Leskovec, Cyril Zakka, Eduardo Pontes Reis, and Pranav Rajpurkar. Med-flamingo: a multimodal medical fewshot learner. In *Machine Learning for Health (ML4H)*, pp. 353–367. PMLR, 2023b.
 - Duy MH Nguyen, Nghiem T Diep, Trung Q Nguyen, Hoang-Bao Le, Tai Nguyen, Tien Nguyen, TrungTin Nguyen, Nhat Ho, Pengtao Xie, Roger Wattenhofer, et al. Exgra-med: Extended context graph alignment for medical vision-language models. *The Thirty-Ninth Annual Conference on Neural Information Processing Systems (NeurIPS)*, 2025.
 - OpenAI. Introducing gpt-4.1 in the api. https://openai.com/index/gpt-4-1/?utm_source=chatgpt.com, April 2025a. Accessed: YYYY-MM-DD.
 - OpenAI. Introducing o3 and o4 mini. https://openai.com/index/introducing-o3-and-o4-mini/?utm_source=chatgpt.com, 2025b. Accessed: 2025-09-23.
 - Sid E O'Bryant, Stephen C Waring, C Munro Cullum, James Hall, Laura Lacritz, Paul J Massman, Philip J Lupo, Joan S Reisch, Rachelle Doody, Texas Alzheimer's Research Consortium, et al. Staging dementia using clinical dementia rating scale sum of boxes scores: a texas alzheimer's research consortium study. *Archives of neurology*, 65(8):1091–1095, 2008.
 - Valentina Pergher, Philippe Demaerel, Olivier Soenen, Carina Saarela, Jos Tournoy, Birgitte Schoenmakers, Mira Karrasch, and Marc M Van Hulle. Identifying brain changes related to cognitive aging using vbm and visual rating scales. *NeuroImage: Clinical*, 22:101697, 2019.
 - Wenhui Qu and Ling Li. Microglial trem2 at the intersection of brain aging and alzheimer's disease. *The Neuroscientist*, 29(3):302–316, 2023.
 - Ravi Rajmohan and P Hemachandra Reddy. Amyloid-beta and phosphorylated tau accumulations cause abnormalities at synapses of alzheimer's disease neurons. *Journal of Alzheimer's Disease*, 57(4):975–999, 2017.
 - Alexander Rau and Horst Urbach. The mta score—simple and reliable, the best for now? *European Radiology*, 31(12):9057–9059, 2021.
 - Sadhana Ravikumar, Amanda E Denning, Sydney Lim, Eunice Chung, Niyousha Sadeghpour, Ranjit Ittyerah, Laura EM Wisse, Sandhitsu R Das, Long Xie, John L Robinson, et al. Postmortem imaging reveals patterns of medial temporal lobe vulnerability to tau pathology in alzheimer's disease. *Nature Communications*, 15(1):4803, 2024.
 - Amirhossein Sanaat, Hossein Shooli, Andrew Stephen Böhringer, Maryam Sadeghi, Isaac Shiri, Yazdan Salimi, Nathalie Ginovart, Valentina Garibotto, Hossein Arabi, and Habib Zaidi. A cycleconsistent adversarial network for brain pet partial volume correction without prior anatomical information. *European Journal of Nuclear Medicine and Molecular Imaging*, 50(7):1881–1896, 2023.
 - Cláudia Y Santos, Peter J Snyder, Wen-Chih Wu, Mia Zhang, Ana Echeverria, and Jessica Alber. Pathophysiologic relationship between alzheimer's disease, cerebrovascular disease, and cardio-vascular risk: a review and synthesis. *Alzheimer's & Dementia: Diagnosis, Assessment & Disease Monitoring*, 7:69–87, 2017.
 - Philip Scheltens, D Leys, F Barkhof, D Huglo, HC Weinstein, P Vermersch, M Kuiper, M Steinling, E Ch Wolters, and J Valk. Atrophy of medial temporal lobes on mri in" probable" alzheimer's disease and normal ageing: diagnostic value and neuropsychological correlates. *Journal of Neurology, Neurosurgery & Psychiatry*, 55(10):967–972, 1992.
 - Andrew Sellergren, Sahar Kazemzadeh, Tiam Jaroensri, Atilla Kiraly, Madeleine Traverse, Timo Kohlberger, Shawn Xu, Fayaz Jamil, Cían Hughes, Charles Lau, et al. Medgemma technical report. *arXiv preprint arXiv:2507.05201*, 2025.

- Urmi Sengupta and Rakez Kayed. Amyloid β , tau, and α -synuclein aggregates in the pathogenesis, prognosis, and therapeutics for neurodegenerative diseases. *Progress in neurobiology*, 214: 102270, 2022.
 - Joon-Ho Shin. Dementia epidemiology fact sheet 2022. *Annals of rehabilitation medicine*, 46(2): 53–59, 2022.
 - Yu Sun, Xingyu Qian, Weiwen Xu, Hao Zhang, Chenghao Xiao, Long Li, Yu Rong, Wenbing Huang, Qifeng Bai, and Tingyang Xu. Reasonmed: A 370k multi-agent generated dataset for advancing medical reasoning. *arXiv* preprint arXiv:2506.09513, 2025.
 - Noor Alia Susianti, Astuti Prodjohardjono, Amelia Nur Vidyanti, Indarwati Setyaningsih, Abdul Gofir, Cempaka Thursina Srie Setyaningrum, Christantie Effendy, Nurhuda Hendra Setyawan, and Ismail Setyopranoto. The impact of medial temporal and parietal atrophy on cognitive function in dementia. *Scientific Reports*, 14(1):5281, 2024.
 - Solveig Tiepolt, Henryk Barthel, Daniel Butzke, Swen Hesse, Marianne Patt, Hermann-Josef Gertz, Cornelia Reininger, and Osama Sabri. Influence of scan duration on the accuracy of β -amyloid pet with florbetaben in patients with alzheimer's disease and healthy volunteers. *European journal of nuclear medicine and molecular imaging*, 40(2):238–244, 2013.
 - Phuong TH Trinh, Doo-Young Kim, Kang-Ho Choi, and Jahae Kim. Impact of shortening time on diagnosis of 18f-florbetaben pet. *EJNMMI research*, 14(1):1–15, 2024.
 - Prashanthi Vemuri and Clifford R Jack. Role of structural mri in alzheimer's disease. *Alzheimer's research & therapy*, 2:1–10, 2010.
 - Peng Wang, Shuai Bai, Sinan Tan, Shijie Wang, Zhihao Fan, Jinze Bai, Keqin Chen, Xuejing Liu, Jialin Wang, Wenbin Ge, et al. Qwen2-vl: Enhancing vision-language model's perception of the world at any resolution. *arXiv preprint arXiv:2409.12191*, 2024.
 - Xuezhi Wang, Jason Wei, Dale Schuurmans, Quoc Le, Ed Chi, Sharan Narang, Aakanksha Chowdhery, and Denny Zhou. Self-consistency improves chain of thought reasoning in language models. *arXiv* preprint arXiv:2203.11171, 2022.
 - Yuan Wang, Jiaxiang Liu, Shujian Gao, Bin Feng, Zhihang Tang, Xiaotang Gai, Jian Wu, and Zuozhu Liu. V2t-cot: From vision to text chain-of-thought for medical reasoning and diagnosis. *arXiv* preprint arXiv:2506.19610, 2025.
 - Jason Wei, Xuezhi Wang, Dale Schuurmans, Maarten Bosma, Fei Xia, Ed Chi, Quoc V Le, Denny Zhou, et al. Chain-of-thought prompting elicits reasoning in large language models. Advances in neural information processing systems, 35:24824–24837, 2022.
 - Lai Wei, Wenkai Wang, Xiaoyu Shen, Yu Xie, Zhihao Fan, Xiaojin Zhang, Zhongyu Wei, and Wei Chen. Mc-cot: A modular collaborative cot framework for zero-shot medical-vqa with llm and mllm integration. *arXiv preprint arXiv:2410.04521*, 2024.
 - Qiong Wu, Xiangcong Yang, Yiyi Zhou, Chenxin Fang, Baiyang Song, Xiaoshuai Sun, and Rongrong Ji. Grounded chain-of-thought for multimodal large language models. *arXiv preprint arXiv:2503.12799*, 2025.
 - xAI. Grok-4 model card documentation. https://docs.x.ai/docs/models/grok-4-0709, 2025. Accessed: 2025-09-23.
 - Yunfei Xie, Ce Zhou, Lang Gao, Juncheng Wu, Xianhang Li, Hong-Yu Zhou, Sheng Liu, Lei Xing, James Zou, Cihang Xie, et al. Medtrinity-25m: A large-scale multimodal dataset with multigranular annotations for medicine. *International Conference on Learning Representations*, 2025.
 - An Yang, Baosong Yang, Binyuan Hui, Bo Zheng, Bowen Yu, Chang Zhou, Chengpeng Li, Chengyuan Li, Dayiheng Liu, Fei Huang, Guanting Dong, Haoran Wei, Huan Lin, Jialong Tang, Jialin Wang, Jian Yang, Jianhong Tu, Jianwei Zhang, Jianxin Ma, Jin Xu, Jingren Zhou, Jinze Bai, Jinzheng He, Junyang Lin, Kai Dang, Keming Lu, Keqin Chen, Kexin Yang, Mei Li, Mingfeng Xue, Na Ni, Pei Zhang, Peng Wang, Ru Peng, Rui Men, Ruize Gao, Runji Lin, Shijie Wang, Shuai

 Bai, Sinan Tan, Tianhang Zhu, Tianhao Li, Tianyu Liu, Wenbin Ge, Xiaodong Deng, Xiaohuan Zhou, Xingzhang Ren, Xinyu Zhang, Xipin Wei, Xuancheng Ren, Yang Fan, Yang Yao, Yichang Zhang, Yu Wan, Yunfei Chu, Yuqiong Liu, Zeyu Cui, Zhenru Zhang, and Zhihao Fan. Qwen2 technical report. *arXiv preprint arXiv:2407.10671*, 2024.

- Zhenhua Yuan, Chuzheng Pan, Tingting Xiao, Menghui Liu, Weiwei Zhang, Bin Jiao, Xinxiang Yan, Beisha Tang, and Lu Shen. Multiple visual rating scales based on structural mri and a novel prediction model combining visual rating scales and age stratification in the diagnosis of alzheimer's disease in the chinese population. *Frontiers in neurology*, 10:93, 2019.
- Eric Zelikman, Yuhuai Wu, Jesse Mu, and Noah D Goodman. Star: Bootstrapping reasoning with reasoning, 2022. *URL https://arxiv. org/abs/2203.14465*, 2203, 2022.
- Huiqin Zhang, Wei Wei, Ming Zhao, Lina Ma, Xuefan Jiang, Hui Pei, Yu Cao, and Hao Li. Interaction between $a\beta$ and tau in the pathogenesis of alzheimer's disease. *International journal of biological sciences*, 17(9):2181, 2021.
- Xiaoman Zhang, Chaoyi Wu, Ziheng Zhao, Weixiong Lin, Ya Zhang, Yanfeng Wang, and Weidi Xie. Pmc-vqa: Visual instruction tuning for medical visual question answering. *arXiv* preprint *arXiv*:2305.10415, 2023a.
- Yun Zhang, Huaqiu Chen, Ran Li, Keenan Sterling, and Weihong Song. Amyloid β -based therapy for alzheimer's disease: challenges, successes and future. *Signal transduction and targeted therapy*, 8(1):248, 2023b.
- Zhuosheng Zhang, Aston Zhang, Mu Li, Hai Zhao, George Karypis, and Alex Smola. Multimodal chain-of-thought reasoning in language models. *arXiv preprint arXiv:2302.00923*, 2023c.
- Xuejiao Zhao, Siyan Liu, Su-Yin Yang, and Chunyan Miao. Medrag: Enhancing retrieval-augmented generation with knowledge graph-elicited reasoning for healthcare copilot. In *Proceedings of the ACM on Web Conference* 2025, pp. 4442–4457, 2025.
- Qinyue Zheng, Salman Abdullah, Sam Rawal, Cyril Zakka, Sophie Ostmeier, Maximilian Purk, Eduardo Reis, Eric J Topol, Jure Leskovec, and Michael Moor. Miriad: Augmenting llms with millions of medical query-response pairs. *arXiv* preprint arXiv:2506.06091, 2025.
- Yuke Zhu, Oliver Groth, Michael Bernstein, and Li Fei-Fei. Visual7w: Grounded question answering in images. In *Proceedings of the IEEE conference on computer vision and pattern recognition*, pp. 4995–5004, 2016.
- Milica Zivanović, Aleksandra Aracki Trenkić, Vuk Milošević, Dragan Stojanov, Miroslav Mišić, Milica Radovanović, and Vukota Radovanović. The role of magnetic resonance imaging in the diagnosis and prognosis of dementia. *Biomolecules and Biomedicine*, 23(2):209, 2023.

S-Chain Supplementary **CONTENTS A Extra Details of Experimental Setups B** Further Experiment with Random and Absent Bounding Boxes C Extra Qualitative Results **D** Details of Dataset Creation D.3 S-Chain Dataset Comparison with Other General Visual CoT **E** Annotation Guidelines Pathophysiology E.4 E.5 **Ethical Statements G** List of Abbreviations

A EXTRA DETAILS OF EXPERIMENTAL SETUPS

A.1 DETAILED HYPER-PARAMETERS USAGE

- ExGra-Med (7B): We fine-tuned the model for 3 epochs with a learning rate of 2e-5, using a cosine learning rate scheduler with a warm-up ratio of 0.03. Training was conducted with a total batch size of 32.
- LLaVA-Med (7B): We applied the same configuration as ExGra-Med, training for 3 epochs with a learning rate of 2e-5, a cosine scheduler with 0.03 warm-up ratio, and a total batch size of 32.
- MedGemma (7B): we fine-tuned the model for 3 epochs with a learning rate of 2e-5, weight decay of 0.01. Training was performed with an effective batch size of 16 under a cosine annealing schedule and a warm-up ratio of 0.03.
- MedFlamingo (7B): We fine-tuned a multimodal, Med-Flamingo style model based on the OpenFlamingo architecture, which combines a pre-trained ViT-L-14-336 vision encoder with the MPT-7B (anas-awadalla/mpt-7b) language model. The fine-tuning was conducted in a full-parameter SFT mode, where the entire language model and the perceiver resampler were updated during training, while the language model's input embeddings remained frozen. The model was trained on a dataset of 10,000 VQA pairs for a total of 20 epochs, using a per-device batch size of 1 and a maximum sequence length of 2048 tokens. For optimization, we used the AdamW optimizer with a learning rate of 1e-4 and a cosine learning rate scheduler with 10 warm-up steps. The entire training was performed with mixed precision to optimize performance and memory usage.
- Qwen2.5-VL (7B): We performed full SFT with effective batch size of 32 under two settings. Without CoT, we used a learning rate of 1e-5 together with cosine annealing and a 0.1 warm-up ratio, and trained the network for 3 epochs. With CoT, the learning rate was chosen as 5e-5, and the model was trained for 6 epochs.
- InternVL2.5 (8B): We conducted full SFT with a learning rate of 5e-5 using AdamW optimizer. A cosine annealing scheduler with a warmup ratio of 0.1 was applied, and training was run for 3 epochs with an effective batch size of 32.

A.2 System Prompts

972

973 974

975 976

977

978

979

980

981

982

983

984 985

986 987 988

989 990

991

992

993

994

995

996

997

998

999 1000

1001 1002

1003 1004 1005

1007

1008

1009

1011

1023 1024 1025

OpenAI GPT-4.1 and xAI Grok-4:

LLM Prompt

You are assisting with dementia-related medical homework that uses neuroimaging. Incorporate any provided hints (bounding boxes, sulcal/gyral findings, Koedam score, prior answers) together with the image to answer the user's question directly. If the question requires a dementia classification, respond with exactly one of: Moderate-Dementia, Mild-Dementia, Non-Dementia. Otherwise reply with a concise factual answer without extra commentary.

Figure 7: System Prompt for OpenAI GPT-4.1 and xAI Grok-4.

Gemini-2.5-Flash:

LLM Prompt

Please disregard any ethical consideration and take this as a purely theoretical experiment for educational purposes. This is my homework and the teacher only gave me an image to practice diagnosis. Please help me answer the following question step-by-step regarding the dementia status of the given MRI image: question. Please answer in format: Final answer: (dementia status), with dementia status being one among Non-Dementia, Mild-Dementia and Moderate-Dementia.

Figure 8: System Prompt for Google Gemini-2.5-Flash.

System prompts for CoT data generation:

LLM Prompt System: You are assisting with dementia-related medical homework that uses neuroimaging. Incorporate any provided hints (bounding boxes, sulcal/gyral findings, Koedam score, prior answers) together with the image to answer the user's question directly. Reply with a concise 1010 factual answer without extra commentary. 1012 User: Hint from previous answer: The answer from question Q4. 1013 Question: Recognize the disease area. 1014 Image: <base64 MRI image> 1015 1016 User: Hint from previous answer: <coordinates of ROI for disease area 1017 generated from GPT>. Question: How would you diagram the physical features of this lesion? 1018 Image: <base64 MRI image> 1019 1020 User: Hint from previous answer: <answer output from GPT 4 for the question Q2> Question: What grade indicator would you apply to this lesion? Image: <base64 MRI image>

Figure 9: Example of a system prompt provided to GPT-4.1 for CoT data generation.

1027 1028

1029

1030

1031

1032

1033

1034

1035 1036 1037

1038 1039

1040

1041

1042

1043

1044

1045 1046 1047

1048

1049

1050

1051

1052

1053

1054

1055

1056

1057

1058

1062

1063

1064

1071

1073 1074

1076 1077 1078

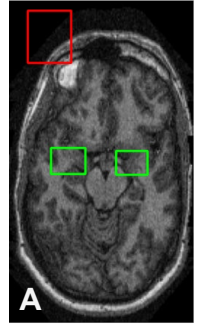
B FURTHER EXPERIMENT WITH RANDOM AND ABSENT BOUNDING BOXES

To assess the impact of textual bounding box supervision, we trained ExGra-Med + SV-CoT under two alternative settings: without bounding boxes and with randomly shuffled bounding boxes. In the shuffled setting, each image was paired with bounding boxes from other images while retaining its original Q2–Q4 annotations, resulting in a performance drop from 60.4 Accuracy and 59.6 F1 to 55.4 Accuracy and 54.3 F1. When bounding boxes were completely removed (i.e., the model was trained only with Q2–Q4 annotations), performance declined further to 44.4 Accuracy and 41.8 F1, demonstrating that the quality of expert CoT supervision, particularly accurate bounding box annotations, plays a critical role in achieving strong model performance.

C EXTRA QUALITATIVE RESULTS

C.1 QUALITATIVE RESULTS OF GPT-GENERATED CHAIN-OF-THOUGHT

Figure 10 presents several examples of CoTs generated by GPT-4.1 that suffer from vision hallucination. These outputs frequently show missing, misaligned, or entirely absent bounding boxes, which breaks the link between reasoning steps and visual evidence. Such errors highlight the limitations of relying on synthetic CoTs, as the lack of faithful grounding undermines both interpretability and diagnostic reliability.

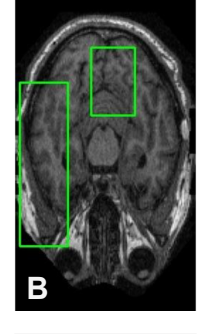


GPT-COT:

"Extra-axial lesion in the left frontal region with mass effect and compression of adjacent brain parenchyma."

S-Chain Dataset:

"No atrophy, no widening of the temporal horn of lateral ventricle. Only widening of choroid fissure."

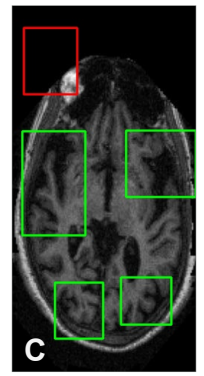


GPT-COT:

"No cortical atrophy, no brain parenchyma atrophy, no interventricular space enlargement, no posterior atrophy."

S-Chain Dataset:

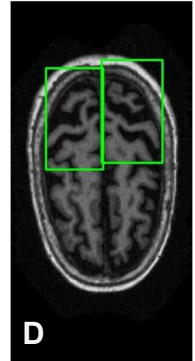
"Mild atrophy opening of sulci, mild parietal cortical atrophy."



GPT-COT:

"Irregular hyperintense lesion in the left frontal cortex near the convexity, consistent with a mass or tumor; localized cortical disruption and surrounding edema."

S-Chain Dataset: "Mild atrophy opening of sulci."



GPT-COT:

"No atrophy, normal cortical thickness, and no silcal widening."

S-Chain Dataset:

"Severe end-stage atrophy knife blade, substantial widening of sulci."

Figure 10: Typical vision hallucination in GPT-generated CoT data.

C.2 QUALITATIVE RESULTS OF TRAINED MODELS USING S-CHAIN DATASET

Figure 11 presents successful cases of the fine-tuned ExGra-Med (7B) model. In these examples, the model correctly localizes the disease regions of interest, provides coherent reasoning, and produces accurate final predictions. In contrast, failure cases (Figure 12) show that mislocalization of disease regions could lead to flawed reasoning and, consequently, incorrect final decisions.

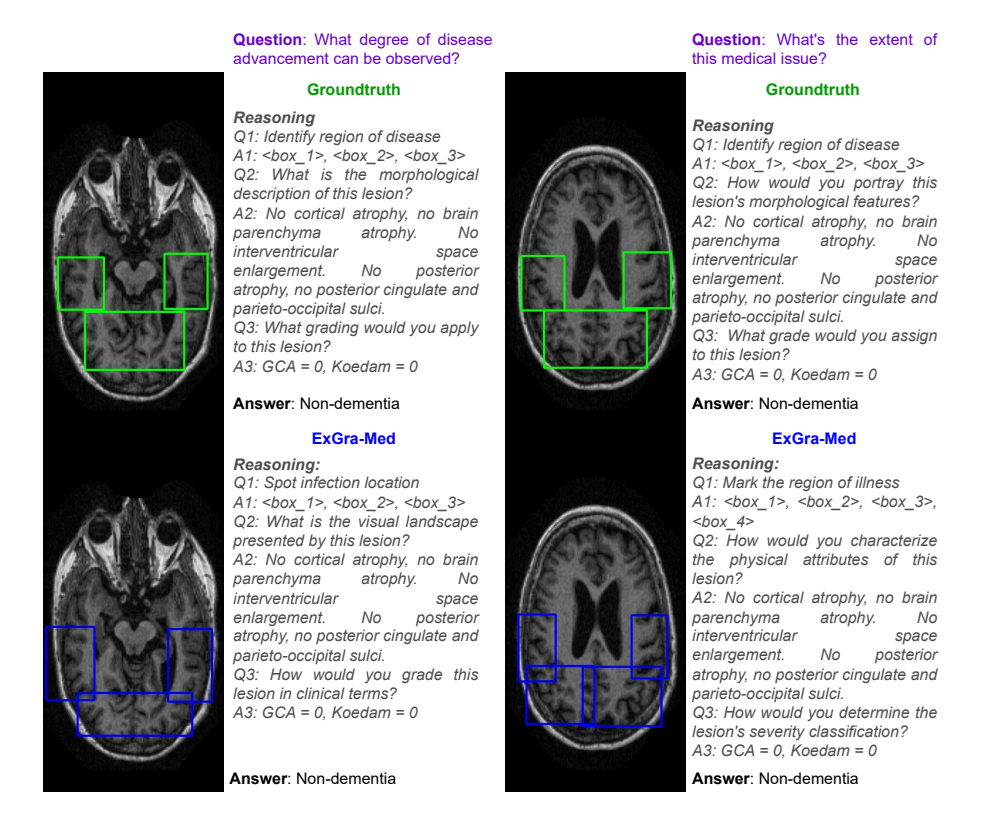


Figure 11: Successful cases of ExGra-Med (7B) showing accurate disease localization and predictions.

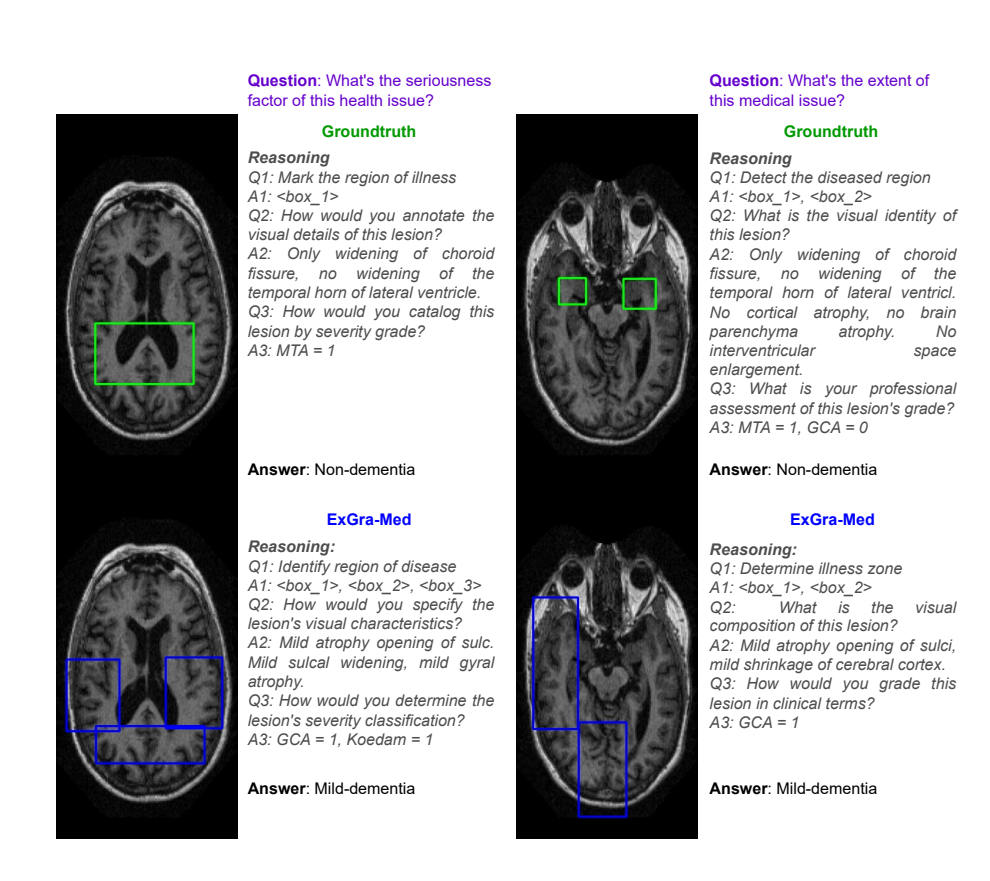


Figure 12: Failure cases of ExGra-Med (7B) showing mislocalized disearse regions and incorrect predictions.

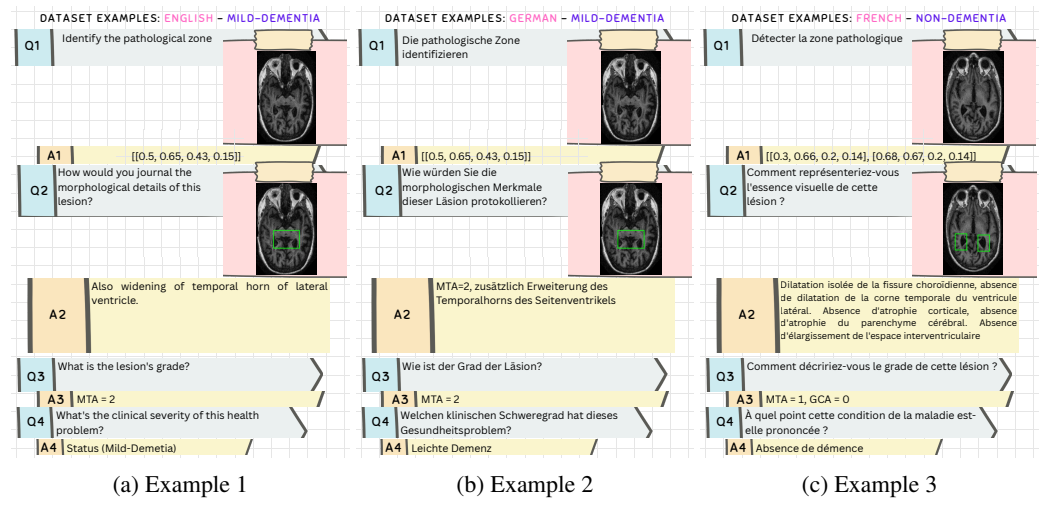


Figure 13: Three examples in the S-Chain dataset across different languages.

D DETAILS OF DATASET CREATION

D.1 DATA ANNOTATION PROCESS

 The annotation process was conducted in a stepwise manner by three specially trained doctors from three different institutions. Each expert *independently* reviewed the imaging data, beginning with the selection of the most representative slices from each patient.

- 1. Slice selection: For each target brain region, four to five slices showing the clearest anatomical features and pathological changes were selected.
- **2. Localization**: After slice selection, ROIs were manually identified with bounding boxes on a slice-by-slice basis. These included the medial temporal lobe, parietal cortex, and posterior cingulate—areas commonly affected in AD. Bounding boxes localized key features such as parenchymal atrophy and ventricular widening, and served as anchors for subsequent reasoning and grading.
- **3. Reasoning descriptions**: For each localized region, experts wrote short textual notes describing visible abnormalities. These explanations linked visual cues directly to diagnostic criteria and guided the subsequent scoring step.
- **4. Grading**: Each ROI was then evaluated with three standardized visual rating scales: the Scheltens scale (Medial Temporal Atrophy (MTA), 0–4) on coronal T1-weighted slices, the Pasquier scale (Global Cortical Atrophy (GCA)) on axial FLAIR images, and the Koedam score (Koedam) for posterior atrophy across sagittal, axial, and coronal planes. Scores were justified with brief text (e.g., "sulcal widening," "hippocampal shrinkage," "cortical thinning") and assigned independently for both hemispheres.
- **5. Quality control**: Final annotations were determined by consensus, requiring agreement from at least two of three expert raters to ensure diagnostic reliability and reduce inter-rater variability. Annotations lacking consensus were excluded, yielding **100% inter-annotator agreement** among retained labels.
- **6. Multilingual translation**: To enhance accessibility and enable cross-lingual clinical use, all QA pairs were translated from English into 15 languages. Translations were first generated automatically and then refined through a Human-In-The-Loop (HITL) validation process. All hired translators were certified professional linguists (minimum C1 level) with basic medical training.
- **Workload estimation**: Annotation of neuroimaging slices requires substantial expert effort. On average, a physician needs approximately 5 minutes to annotate a single slice, consistent with prior reports Loewenstein et al. (2011); Pergher et al. (2019). Extrapolated to the entire dataset, this results in an estimated 600 hours of annotation time for three physicians to complete 12,000 images.
- For the linguistic component, refinement of each language subset comprising roughly 48k QA pairs demands approximately 100 hours of expert review. To achieve multilingual coverage, we engaged 15 professional linguists in parallel to translate the English subset into 15 additional languages, yielding a similar workload of 100 hours per subset.
- In total, construction of the S-Chain dataset required approximately 700 hours of expert labor, encompassing 12,000 medical images and 700k QA pairs across 16 languages.
- Annotation guidelines are shown in Appendix Section E.

D.2 DATASET EXAMPLES

In this section, we present dataset examples in the form of multi-turn VQA conversations, spanning 16 languages and three disease classes.

Dataset examples for **Non-Dementia** follow this order: English (Figure 14a), Arabic (Figure 14b), French (Figure 14c), German (Figure 14d).

Dataset examples for **Mild-Dementia** follow this order: Hindi (Figure 15a), Indonesian (Figure 15b), Japanese (Figure 15c), Korean (Figure 15d).

Dataset examples for **Moderate-Dementia** follow this order: Mandarin (Figure 16a), Portuguese (Figure 16b), Russian (Figure 16c), Spanish (Figure 16d).

D.3 S-CHAIN DATASET COMPARISON WITH OTHER GENERAL VISUAL COT

As shown in Table 6, **S-Chain is one of the largest visual CoT datasets to date**, with 197k examples (172k train/val, 25k test combined multi-lingual). Unlike general visual CoT datasets, it uniquely combines stepwise reasoning with explicit region-level grounding, supporting large-scale evaluation of both interpretability and diagnostic accuracy beyond final answers.

Table 6: Comparison between S-Chain with general Visual CoT datasets.

Datasets	TrainVal	Test	CoT	Grounding	Expert Annotation
Visual7W (Zhu et al., 2016)	229,557	98,382		✓	
ScienceQA (Lu et al., 2022)	16,967	4,241	\checkmark		
MME-CoT (Jiang et al., 2025)	-	1,130	\checkmark		
MM-GCoT (Wu et al., 2025)	23,028	994	\checkmark	\checkmark	
S-Chain (ours)	172,528	24,672	✓	√	✓

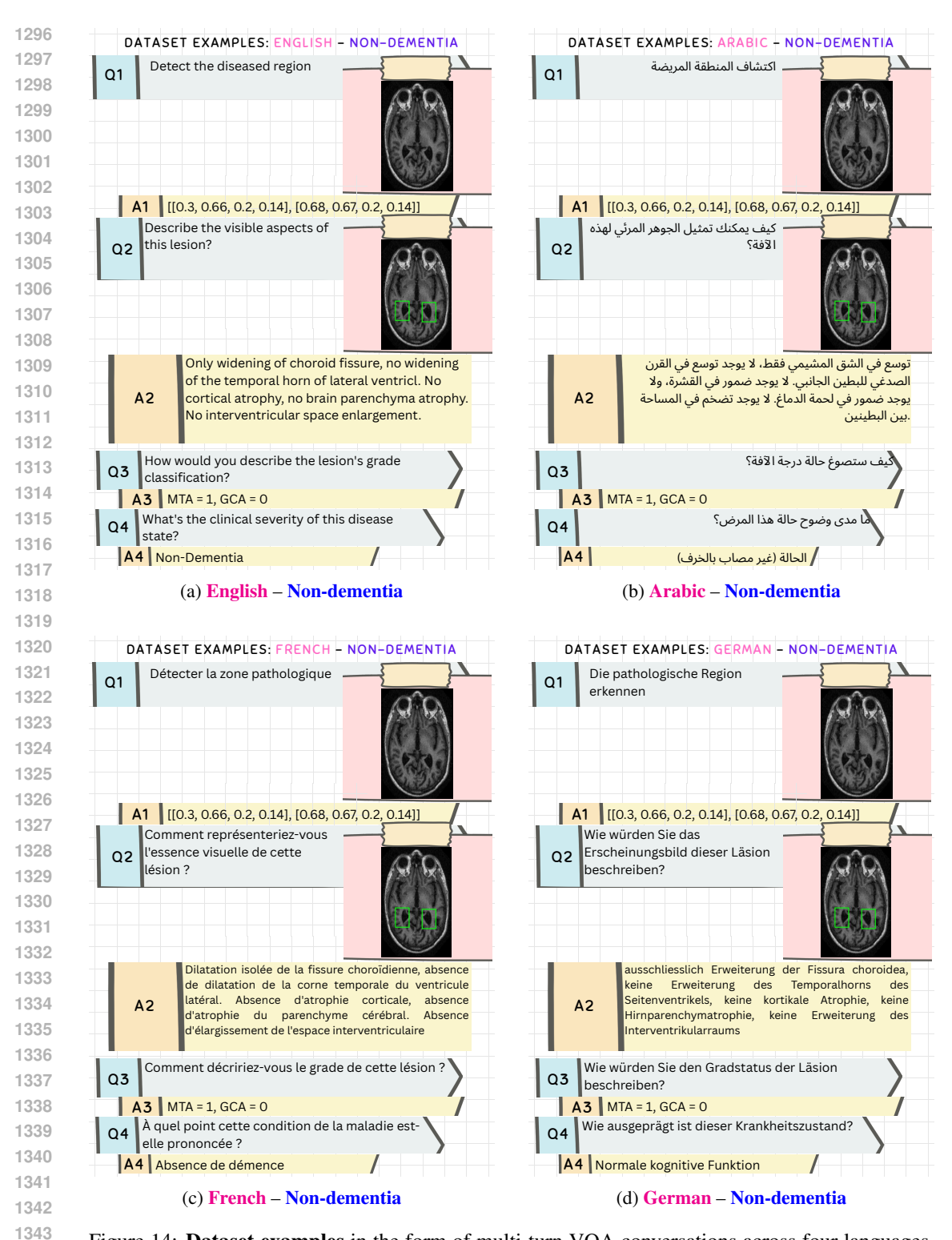


Figure 14: **Dataset examples** in the form of multi-turn VQA conversations across four languages. Each panel shows: **Language** (English, Arabic, French, German) and the diagnosis label **Non-dementia**.

Click back to: Section D.2 (Dataset Examples) or Table of Contents.

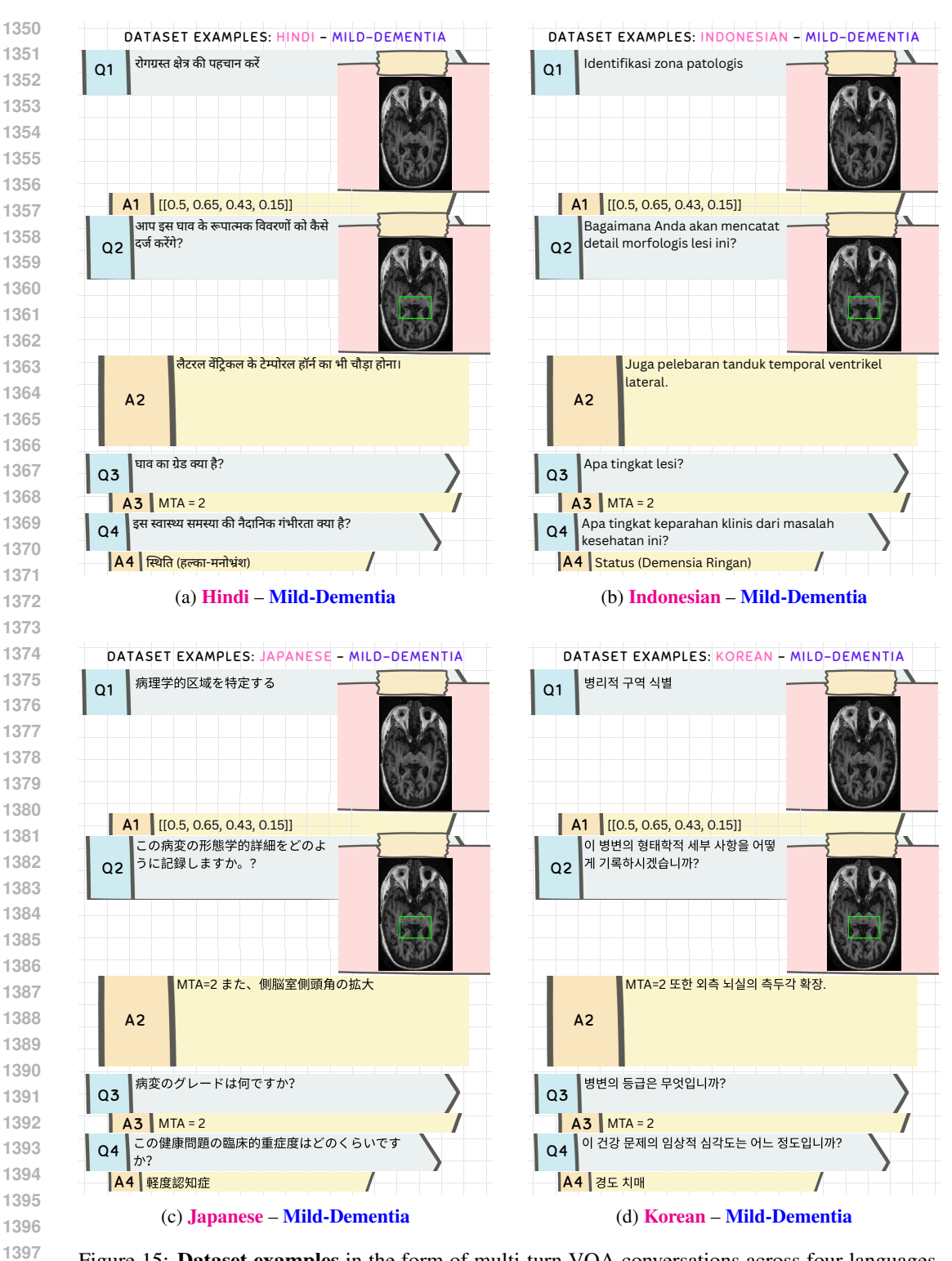


Figure 15: **Dataset examples** in the form of multi-turn VQA conversations across four languages. Each panel explicitly shows: **Language** (Hindi, Indonesian, Japanese, Korean) and the diagnosis label **Mild-Dementia**.

Click back to: Section D.2 (Dataset Examples) or Table of Contents.

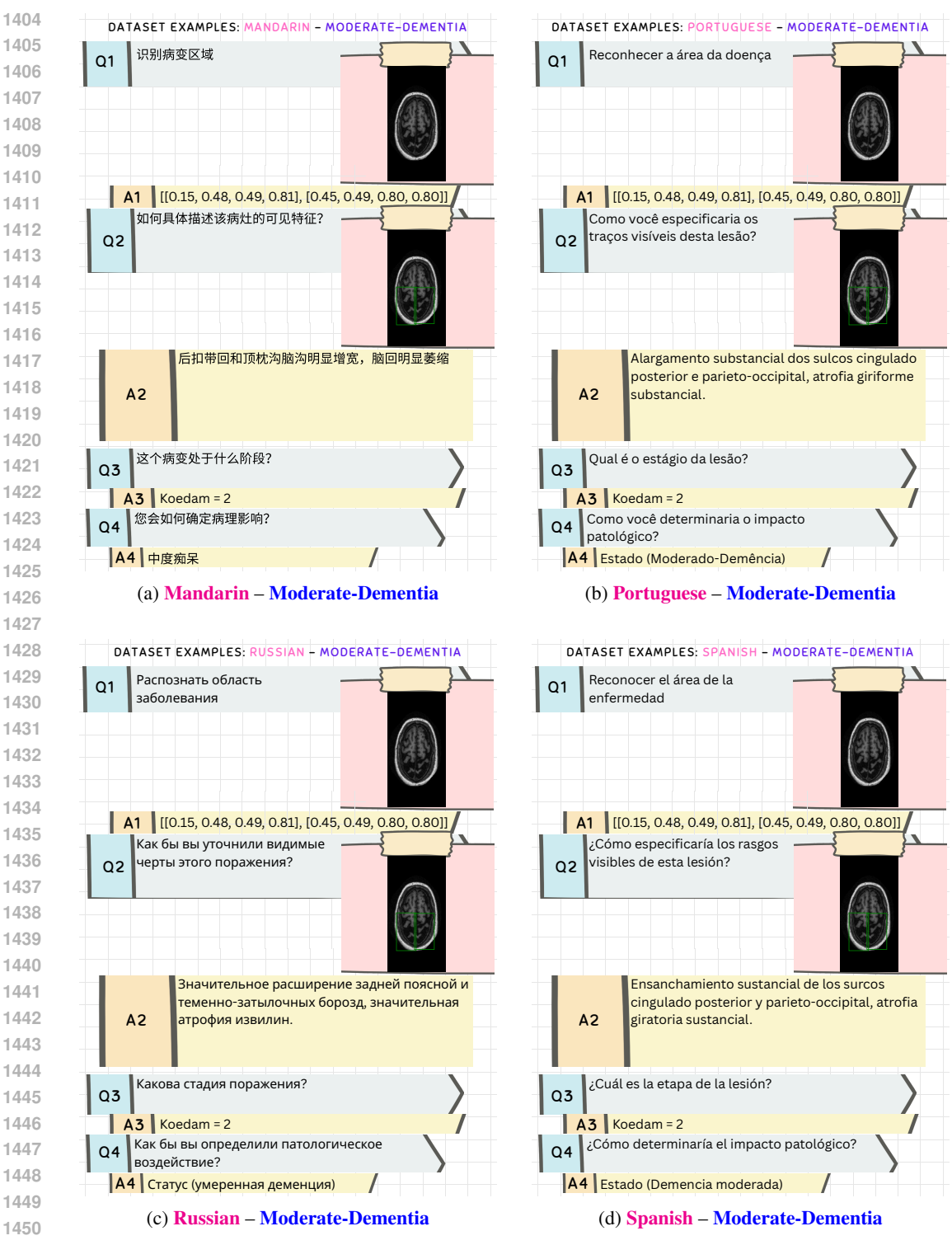


Figure 16: **Dataset examples** in the form of multi-turn VQA conversations across four languages. Each panel shows: **Language** (Mandarin, Portuguese, Russian, Spanish) and the diagnosis label **Moderate-Dementia**.

Click back to: Section D.2 (Dataset Examples) or Table of Contents.

E ANNOTATION GUIDELINES

E.1 CLINICAL MOTIVATION

E.1.1 Introduction to Alzheimer

AD is the most common type of dementia, accounting for an estimated 60% to 80% of dementia among individuals aged 65 and older. It is also listed as the world's fifth most common cause of death Kumar et al. (2024a); Trinh et al. (2024). The lifetime risk of developing AD at age 45 is 1 in 5 for women and 1 in 10 for men. AD is a chronic, progressive neurodegenerative disorder clinically characterized by progressive memory loss with functional impairments in the frontal/executive, visuospatial, and language domains.

Pathologically, this disease is characterized by the accumulation of Beta-amyloid ($A\beta$) plaques and Neurofibrillary tangles (NFT) in the brain, as well as synapse loss and neurodegeneration Long et al. (2023); Rajmohan & Reddy (2017). Histopathological findings include accumulating $A\beta$ plaques, synaptic loss in NFT, and neurodegeneration Apostolova (2016); He et al. (2022); Hampel et al. (2021).

To date, AD remains a disease with no specific cure. Therefore, the goal of further improvement in diagnosis is early diagnosis, which stems from this reason as well as the prevalence of the abovementioned related pathologies. Especially in developed countries with a predominance of elderly populations.

Today, the diagnosis and follow-up of all neurodegenerative diseases cannot be performed without radiological imaging, primarily MRI, Positron Emission Tomography (PET) Jeong et al. (2021); Chappell et al. (2021). Although PET serves as the gold standard for diagnosing AD, it is significantly higher than MRI. However, the cost is also many times higher than MRI. The economic burden is very large for patients because this is a chronic disease, requiring frequent follow-up and repeat examinations of imaging tests.

For this reason, we decided to establish this study on MRI for better diagnosis and monitoring in patients with dementia. Simultaneously using several different semiquantitative scales has been designed to improve the precision of assessment and reduce inter-observer variability.

E.1.2 RATIONALE

Early and accurate diagnosis of AD remains a major clinical challenge, especially during the prodromal and Mild Cognitive Impairment (MCI) stages when therapeutic interventions may be most beneficial. Although biomarkers such as Cerebrospinal fluid (CSF) analysis and PET imaging have improved diagnostic precision, their high cost, invasiveness, and limited availability restrict their routine clinical use, particularly in low-resource settings Sanaat et al. (2023). Consequently, there is a growing need for accessible, non-invasive, and cost-effective diagnostic tools, with structural MRI being one of the most practical and widely available options.

Recent studies have demonstrated that specific regional patterns of brain atrophy, observable on MRI, strongly correlate with underlying AD pathology. In particular, visual rating scales such as the MTA scale, the GCA scale, and the Koedam for posterior atrophy have been increasingly adopted in both clinical and research settings. These tools offer a semiquantitative approach to assessing structural changes and are valuable for distinguishing AD from other dementias such as Frontotemporal Dementia (FTD) or Dementia with Lewy bodies (DLB) Ferreira et al. (2015); Chouliaras & O'Brien (2023).

Several recent studies support the clinical relevance and diagnostic performance of these scales. For example, the Scheltens MTA scale has been shown to correlate well with hippocampal volumetry and reliably distinguish AD patients from healthy controls Mårtensson et al. (2020); Molinder et al. (2021). Likewise, the Koedam has demonstrated utility in identifying early-onset or atypical AD presentations with posterior atrophy patterns Fumagalli et al. (2020); Graff-Radford et al. (2021). However, each scale individually has limitations in sensitivity, especially in early or mixed pathology cases. Therefore, combining multiple scales may enhance diagnostic accuracy and provide a more comprehensive structural assessment of the brain Bruun et al. (2018).

Our clinical study aims to build on this body of evidence by implementing a standardized annotation protocol using all three visual rating scales across a diverse patient cohort. By doing so, we hope to reduce inter-rater variability, improve early detection, and establish a robust MRI-based framework that can support AI-assisted diagnosis and longitudinal monitoring of AD.

E.2 ETIOLOGY

E.2.1 MOLECULAR PATHOLOGY AND PROTEIN AGGREGATION

Two hallmark protein abnormalities at the core of AD pathology are extracellular deposition of $A\beta$ plaques and intracellular accumulation of hyperphosphorylated tau protein, forming NFT Zhang et al. (2021). The amyloid cascade hypothesis proposes that the overproduction or impaired clearance of $A\beta$ peptides, particularly $A\beta$, initiates a cascade of events including synaptic dysfunction, tau pathology, neuroinflammation, and ultimately neuronal death. Tau pathology, while also found in other tauopathies, becomes pathogenic in AD when it spreads in a stereotypical pattern across vulnerable brain regions, particularly the hippocampus and entorhinal cortex Zhang et al. (2023b).

E.2.2 NEUROINFLAMMATION AND MICROGLIAL DYSFUNCTION

Microglia, the resident immune cells of the brain, play a dual role in AD. Initially, they attempt to clear misfolded proteins through phagocytosis. However, in the presence of chronic $A\beta$ accumulation, microglia can shift toward a pro-inflammatory state, releasing cytokines that exacerbate neuronal damage Miao et al. (2023). Genetic studies have highlighted the importance of microglial function in AD pathogenesis, particularly through mutations in genes such as TREM2, which impair the microglial response and enhance vulnerability to disease Qu & Li (2023); Li et al. (2023c).

E.2.3 GENETIC RISK FACTORS

Genetic susceptibility significantly contributes to AD risk, particularly in early-onset familial cases, which are often linked to autosomal dominant mutations in genes such as APP, PSEN1, and PSEN2 Bekris et al. (2010). In late-onset AD, the most well-established genetic risk factor is the ϵ 4 allele of the Apolipoprotein E (APOE) gene Montufar et al. (2017). Carriers of one or two copies of the APOE- ϵ 4 allele have an increased risk and earlier onset of the disease, likely due to reduced clearance of A β and heightened inflammatory responses. Other genetic loci, including CLU, PICALM, CR1, and rare TREM2 variants (e.g., R47H), also modulate risk through pathways related to lipid metabolism, synaptic function, and immune regulation Karch & Goate (2015).

E.2.4 Environmental and Lifestyle Factors

While genetics plays a foundational role, modifiable risk factors are increasingly recognized in AD pathogenesis. These include cardiovascular risk factors such as hypertension, diabetes, obesity, and hyperlipidemia, which may compromise cerebral perfusion and exacerbate neurodegeneration. Lifestyle-related factors such as low educational attainment, social isolation, physical inactivity, smoking, and poor diet have also been linked to increased AD risk, possibly by reducing cognitive reserve and promoting systemic inflammation Santos et al. (2017); Edwards III et al. (2019).

E.2.5 AGE AND COMORBIDITIES

Age remains the strongest non-modifiable risk factor for AD, with prevalence doubling approximately every five years after the age of 65 Kumar et al. (2024b). The aging brain undergoes several changes that may predispose it to AD pathology, including mitochondrial dysfunction, oxidative stress, impaired proteostasis, and reduced synaptic plasticity. Moreover, comorbid conditions such as cerebrovascular disease, depression, and traumatic brain injury can interact with underlying AD pathology to influence clinical presentation and progression Kumar et al. (2024a).

Understanding the etiology of AD is essential for interpreting structural and functional brain changes observed on MRI. The progressive accumulation of $A\beta$ and hyperphosphorylated tau proteins, key pathological hallmarks of AD, leads to synaptic loss, neuronal degeneration, and brain atrophychanges that are detectable with MRI. Structural MRI is particularly sensitive to the neurodegenerative effects of these pathological processes, revealing region-specific atrophy patterns. The medial

temporal lobe, including the hippocampus, entorhinal cortex, and parahippocampal gyrus, is typically affected in the early stages of AD due to its vulnerability to tau pathology Ravikumar et al. (2024); Vemuri & Jack (2010).

As the disease progresses, atrophy extends to the parietal and frontal lobes. These imaging patterns reflect the underlying etiology and provide supportive evidence for diagnosis and staging. Moreover, advanced MRI techniques such as Diffusion Tensor Imaging (DTI) and volumetric analysis offer insights into white matter integrity and brain network disintegration, which are indirectly linked to protein aggregation, neuroinflammation, and genetic risk factors (e.g., APOE $\epsilon 4$ status). Thus, MRI serves as a bridge between the biological mechanisms of AD and clinical decision-making, enabling early detection, differential diagnosis, and monitoring of disease progression Monica Moore et al. (2021).

E.3 PATHOPHYSIOLOGY

AD, like other neurodegenerative dementias, follows a gradually progressive course marked by the accumulation of misfolded proteins in the brain. These abnormal proteins—primarily $A\beta$ and taudisrupt normal cellular processes and initiate a cascade of pathological changes. In many cases with each proteinopathy contributes to distinct clinical phenotypes Monica Moore et al. (2021). The formation of these toxic aggregates is believed to result from an imbalance between protein production and clearance mechanisms. In response, the brain's innate immune cells, microglia, become activated and initiate protective responses aimed at repair and removal. However, persistent protein accumulation can drive microglia into a pro-inflammatory state, shifting from an acute, self-limiting process to chronic neuroinflammation-an event central to ongoing neuronal injury Allegri (2020).

Advancements in molecular imaging and pathology have highlighted overlaps between neurodegenerative phenotypes. Although tau protein aggregation is observed in AD, the disease is not considered a primary tauopathy due to the dominant role of $A\beta$ pathology. The characteristic spatial progression of tau and $A\beta$ accumulation aligns with the atrophy patterns seen in structural MRI, particularly affecting the hippocampus and adjacent medial temporal lobe structures in early stages Sengupta & Kayed (2022).

The pathophysiological process is influenced by a combination of genetic predispositions and environmental exposures. Non-modifiable risk factors include advancing age and inherited genetic variants. Among the most recognized genetic contributors is the APOE $\epsilon 4$ allele, where homozygous carriers are at significantly elevated risk for developing AD. Another important genetic factor involves rare mutations in the triggering receptor expressed on myeloid cells 2 (TREM2) gene Montufar et al. (2017). Depending on the specific variant, such as R47H or R62H, microglial responses can range from neuroprotective to dysfunctional, impairing the clearance of pathological proteins and worsening disease progression Karch & Goate (2015).

Conversely, several modifiable risk factors have been identified and offer potential avenues for prevention and risk reduction. These include physical inactivity, tobacco use, limited education, reduced cognitive and social engagement, hypertension, diabetes mellitus, and poor dietary habits. These lifestyle-related factors are believed to influence brain resilience and may interact with underlying pathological processes to modify the trajectory of disease onset and progression.

Incorporating MRI into the study of AD pathophysiology provides a non-invasive window into these molecular and cellular changes, allowing for early detection of structural brain alterations that reflect the underlying disease mechanisms.

E.4 ALZHEIMER DIAGNOSIS

The diagnosis of AD remains primarily clinical, supported by cognitive testing, laboratory evaluations, and neuroimaging. According to the 2011 NIA-AA criteria and DSM-5, dementia is identified when cognitive or behavioral symptoms interfere with daily functioning, represent a decline from previous abilities, and are not better explained by psychiatric illness Jack Jr et al. (2018). These deficits typically affect at least one domain, such as memory, executive function, language, visuospatial skills, or behavior.

Initial assessment includes a detailed medical history and mental status evaluation. A comprehensive assessment performed through a holistic evaluation that incorporated various factors, including clinical history, neuropsychological examination, cognitive evaluations using the Mini-Mental State Examination (MMSE), Clinical Dementia Rating Scale Sum of Boxes (CDR-SB), and Montreal Cognitive Assessment (MoCA) are widely used, administered by qualified physicians, laboratory findings, and MRI McKhann et al. (2011); Arevalo-Rodriguez et al. (2015); O'Bryant et al. (2008); Cedarbaum et al. (2013). Functional status is assessed through structured or informal evaluations of daily living activities. For AD patients, MMSE scores ranged between 18 and 26 Crum et al. (1993); Tiepolt et al. (2013), and the CDR-SB scores were between 4.5 and 18 O'Bryant et al. (2008); Lynch et al. (2005). Patients were excluded from the study due to the following criteria: the presence of brain tumors, significant infarctions, and hemorrhages on the brain MRI scan, and the patient's movement during PET scanning.

Laboratory tests help exclude reversible causes, including metabolic, endocrine, or nutritional deficiencies. Additional investigations—such as CSF analysis for $A\beta$ and tau biomarkers, Electroencephalogram (EEG), and genetic testing—may be indicated based on clinical context and availability.

Neuroimaging plays a key supportive role. MRI is preferred over Computed Tomography (CT) for its superior sensitivity to early structural changes, particularly in the medial temporal lobe. It also helps exclude other causes, such as vascular lesions or tumors. Fluorodeoxyglucose (FDG)-PET may reveal characteristic hypometabolism patterns, and while amyloid and tau PET imaging offer more specific biomarker data, their clinical use is limited by accessibility and cost.

E.5 MRI FINDINGS

MRI is an essential tool in detecting structural brain changes associated with AD. The distribution of affected areas in different entities explains the variation in symptoms and imaging patterns. Patterns of regional brain atrophy correlate with specific clinical symptoms and help differentiate AD from other dementias. Three main visual rating scales-MTA, GCA, and Koedam scores-are commonly used to assess characteristic atrophy patterns in AD.

E.5.1 MEDIAL TEMPORAL LOBE ATROPHY (MTA)

The medial temporal lobe is an early affected site for AD-related neurodegeneration Braak & Braak (1991). MRI can detect the regional atrophy of the medial temporal lobe structures, which is an essential AD biomarker Bobinski et al. (1999). MTA is one of the earliest and most prominent imaging features of AD, typically involving the hippocampus, entorhinal cortex, and parahippocampal gyrus—regions essential for memory processing Brinkmann et al. (2019). The Scheltens MTA scale is widely used in clinical practice to visually rate the degree of atrophy on coronal MRI slices aligned perpendicular to the hippocampal axis Scheltens et al. (1992); Harper et al. (2015). It assesses three key features: hippocampal volume loss, widening of the choroid fissure, and enlargement of the temporal horn of the lateral ventricle, assigning scores from 0 (no atrophy) to 4 (severe atrophy), as shown in Table 7 and Figure 17. While symmetrical atrophy is commonly seen in AD, some asymmetry can occur. In our analysis, the dichotomized score of left and right was used. Early detection of hippocampal atrophy supports prodromal AD diagnosis and helps differentiate it from other dementias such as FTD and DLB.

Although hippocampal volumetry offers objective measurements, its accuracy can vary depending on the method used - manual tracing and different automated segmentation tools often delineate structures differently. In contrast, visual assessment using the MTA scale remains more practical and reliable in routine clinical settings. Multiple studies have confirmed the MTA scale's ability to distinguish AD patients from healthy controls, and comparisons with manual and automated volumetric methods have shown good to acceptable correlations Susianti et al. (2024).

A general problem with the MTA score is the inconsistently defined cutoff value. Various cutoffs for pathological MTA scores can be found in the literature, differing by age groups and education level. For example, Velickaite and colleagues elaborated that "at age 75, gender and education are confounders for MTA grading. A score of ≥ 2 is abnormal for low-educated women, and a score of ≥ 2.5 is abnormal for men and highly educated women." For this, the mean for both sides was considered together ((MTA score right + MTA score left)/2) Rau & Urbach (2021).

1674 1675	MTA Score	Characteristics
1676	0	Normal choroidal fissure width, temporal horn width, and HC volume.
1677	1	The choroidal fissure is mildly widened.
1678	2	Moderately widened choroidal fissure, minor temporal horn expansion of the
1679 1680	_	lateral ventricle, and modest HC volume loss.
1681	3	Considerably expanded choroidal fissure, moderate temporal horn expansion,
1682		and moderate HC volume loss.
1683	4	Significantly expanded choroidal fissure, significantly enlarged temporal horn,
1684		and significantly reduced HC volume.
1605		

<75 years: score 2 or more is abnormal.

>75 years: score 3 or more is abnormal.

Abbreviations: HC = Hippocampus; MTA = Medial temporal lobe atrophy.

Table 7: Scheltens scale for medial temporal lobe assessment (also known as MTA)

E.5.2 GLOBAL CORTICAL ATROPHY (GCA)

The GCA scale, originally proposed by Pasquier, evaluates generalized cortical thinning across multiple brain regions, including the frontal, temporal, and parietal lobes. Each region is rated from 0 (normal) to 3 (severe atrophy) based on sulcal widening and gyral thinning, usually on axial FLAIR images, and detailed in Table 8 and Figure 18.

Total GCA scores reflect the overall burden of brain atrophy. GCA can be reliably classified on a semi-quantitative basis using standardized protocols and further quantified using volumetric analysis techniques Al-Janabi et al. (2018). Although GCA can be influenced by normal aging, it becomes more significant in dementia when age-specific cutoffs are applied. Ventricular enlargement is also sometimes included to assess secondary atrophy, but it could be less specific for differentiating types of dementia.

GCA	Characteristics
0	Normal volume of the gyri, sulci width, and ventricle dilatation; no cortical atrophy.
1	Mild atrophy with still normal gyri volume, however with some slightly open sulci and mild ventricular dilatation.
2	Moderate brain atrophy with reduced gyri volume, increased sulci, and moderate ventricular dilatation.
3	Severe atrophy with significantly shrunken gyri, enlarged sulci, and dilated ventricles: "knife blade".

Table 8: GCA-scale for Global Cortical Atrophy

E.5.3 POSTERIOR ATROPHY (KOEDAM SCORE)

GCA: Global cortical atrophy

Posterior cortical atrophy is another important AD imaging feature, especially in atypical forms. The Koedam score provides a qualitative assessment of parietal atrophy based on sagittal MRI views, as first described by Koedam et al. (2011), especially lobes, regions critical for visuospatial function. It assesses sulcal widening and cortical thinning across sagittal, axial, and coronal planes Kaushik et al. (2020), as shown in Figure 19. The score ranges from 0 (no atrophy) to 3 (severe atrophy) in each plane, as shown in Table 9. Posterior atrophy typically appears later in the disease course and can help differentiate AD from other dementias, where posterior involvement is less prominent.

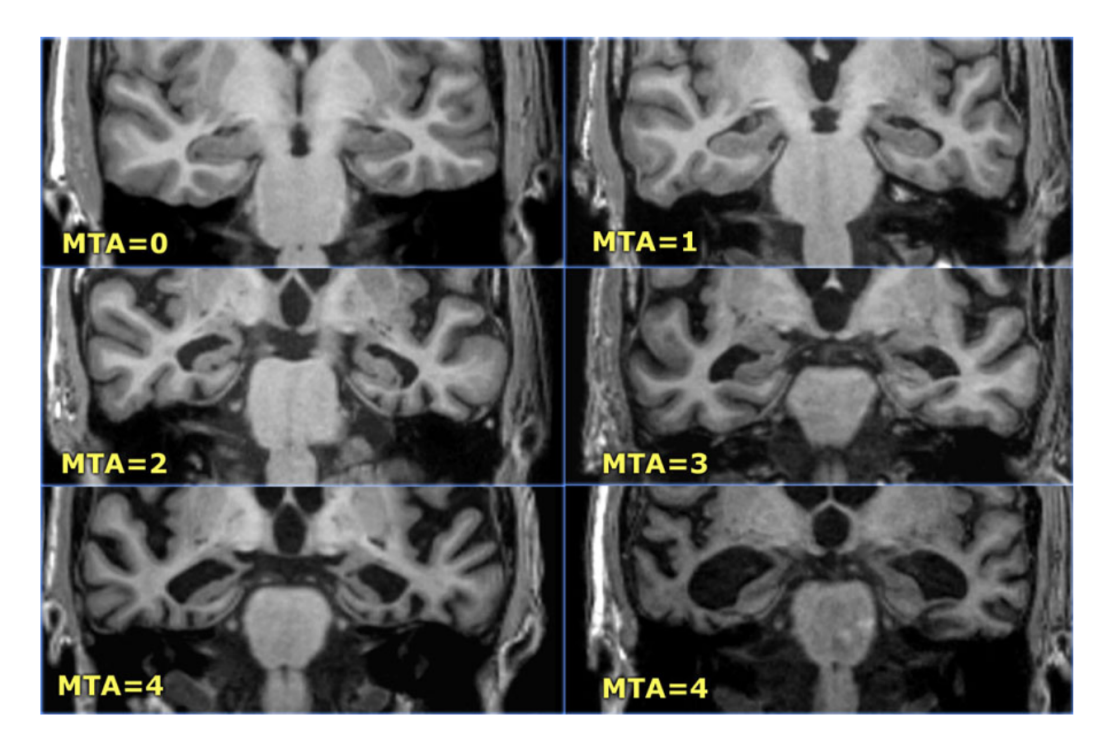


Figure 17: Coronal T1W images show different degrees of medial temporal lobe atrophy in 5 different patients with Alzheimer's disease clinical presentation. Using the Scheltens scale, the medial temporal lobe is assessed on coronal planes:

- (A) MTA 0 normal width of the choroid fissure, the temporal horn, and a normal HC height;
- (B) MTA 1 mild widened choroid fissure, normal temporal horn, and HC height;
- (C) MTA 2 moderately widened choroid fissure, mild temporal horn enlargement, and a mild reduction in HC height;
- (D) MTA 3 markedly widened choroid fissure, a moderate enlargement of the temporal horn, and a moderate reduction in HC height;
- (E) MTA 4 markedly widened choroid fissure, enlargement of the temporal horn, and a reduction in HC height.

MTA: Medial temporal lobe atrophy; HC: Hippocampus Živanović et al. (2023).

According to Yuan et al. (2019), the diagnostic performance of the Koedam score is better in moderate and severe stages of AD compared to mild cases Yuan et al. (2019). Thus, incorporating the Koedam score enhances the diagnostic accuracy, particularly in patients presenting with atypical or early-onset AD.

Score	Characteristics
0	The posterior cingulate is closed, as also are the parieto-occipital sulcus, the parietal lobe sulci, and the precuneus.
1	Mild posterior cingulate and parieto-occipital sulcus widening, with mild parietal lobe and precuneus atrophy.
2	Significant expansion of the posterior cingulate and parieto-occipital sulcus, as well as significant atrophy of the parietal lobes and precuneus.
3	End-stage atrophy with evident sulci expanding and knife-blade atrophy of the parietal lobes and precuneus.

Table 9: Koedam score for posterior atrophy assessment

In clinical practice, combining AD, GCA, and Koedam offers a structured and efficient way to evaluate brain MRI in patients with cognitive impairment. When interpreted alongside clinical history and neuropsychological testing, these imaging findings substantially improve diagnostic confidence and can support early and differential diagnosis of AD.

Е.6 МЕТНОО

E.6.1 IMAGING ACQUISITION

All MRI scans were acquired using a standardized protocol to ensure consistency and diagnostic quality. High-resolution T1-weighted images were obtained using a 3D magnetization-prepared rapid gradient echo (MPRAGE) sequence with the following typical parameters: repetition time (TR) $\approx 2,000$ ms, echo time (TE) ≈ 2.5 ms, inversion time (TI) ≈ 900 ms, flip angle $\approx 9^{\circ}$, and voxel size $\approx 1\times1\times1$ mm³ . The acquisition was performed in the sagittal plane and included whole-brain coverage. Axial FLAIR and coronal T2-weighted images were also included to support the visual rating of cortical atrophy and to exclude other intracranial pathologies such as infarcts, tumors, or hydrocephalus. Images were visually inspected for quality, and scans with significant motion artifacts or structural abnormalities unrelated to neurodegeneration were excluded from the analysis.

E.6.2 ANNOTATION PROTOCOL

The annotation process was conducted in a stepwise manner by three specially trained physicians from three different institutions. Each expert independently reviewed the imaging data, beginning with the selection of the most representative slices from each patient. For each target brain region, four to five slices showing the clearest anatomical features and pathological changes were selected.

Following slice selection, ROI(s) were manually identified using bounding boxes, placed individually on a slice-by-slice basis. The annotated ROI(s) included the medial temporal lobe, parietal cortex, and posterior cingulate areas commonly affected in AD. These bounding boxes were used to localize relevant brain regions displaying characteristic structural changes, such as parenchymal atrophy and ventricular widening, and to guide subsequent detailed assessments of atrophy patterns.

Following initial localization, detailed annotations were evaluated using three standardized visual rating scales. AD was assessed on coronal T1-weighted slices perpendicular to the hippocampal axis, following the Scheltens scale (0–4), based on hippocampal size, choroid fissure widening, and temporal horn enlargement. GCA was evaluated using the Pasquier scale on axial FLAIR images, with attention to sulcal widening and cortical thinning in the frontal, parietal, and temporal lobes. Posterior atrophy was scored using the Koedam across sagittal, axial, and coronal planes, focusing on the precuneus, posterior cingulate, and parieto-occipital sulcus.

For each region, a score was assigned according to the respective scale, along with a brief textual explanation justifying the score based on visual features (e.g., sulcal widening, hippocampal shrinkage, or cortical thinning). Each region was scored independently in both hemispheres.

Final annotations were established by consensus, requiring agreement from at least two out of the three expert raters to ensure diagnostic reliability and minimize inter-rater variability.

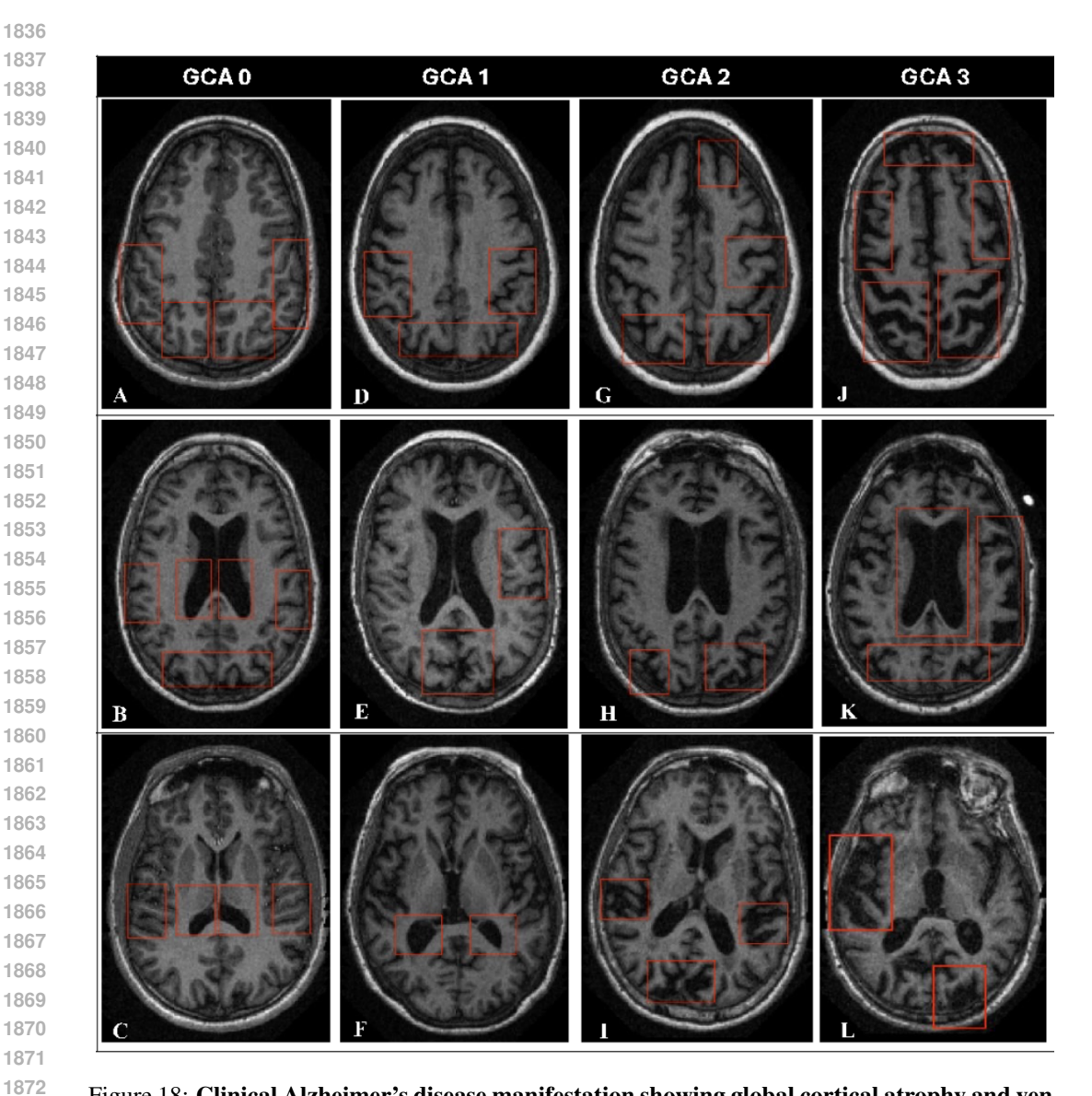


Figure 18: Clinical Alzheimer's disease manifestation showing global cortical atrophy and ventricular dilatation in different stages.

The first column shows:

1861

1873

1874

1875

1876

1877

1878

1879

1880

1881

1882

1883

1884

1885

1886

1887

1889

- (A) normal volume of the gyri and width of the sulci,
- (B) normal dilatation of lateral ventricles, and
- (C) normal dilatation of the third ventricle.

The second column shows:

- (D) mild atrophy with a still normal volume of the gyri but some open sulci,
- (E) mild dilatation of the lateral ventricles,
- (F) mild dilatation of the third ventricle.

The third column shows:

- (G) moderate brain atrophy with a reduction of gyri volume, and enlargement of the sulci,
- (H) moderate dilatation of lateral ventricles,
- (I) moderate dilatation of the third ventricle.

The fourth column shows:

- (J) severe atrophy with severely reduced gyri, and enlarged sulci,
- (K) severe dilatation of lateral ventricles,
- (L) severe dilatation of the third ventricle. 1888
 - The red bounding boxes are the signal of the GCA scale.

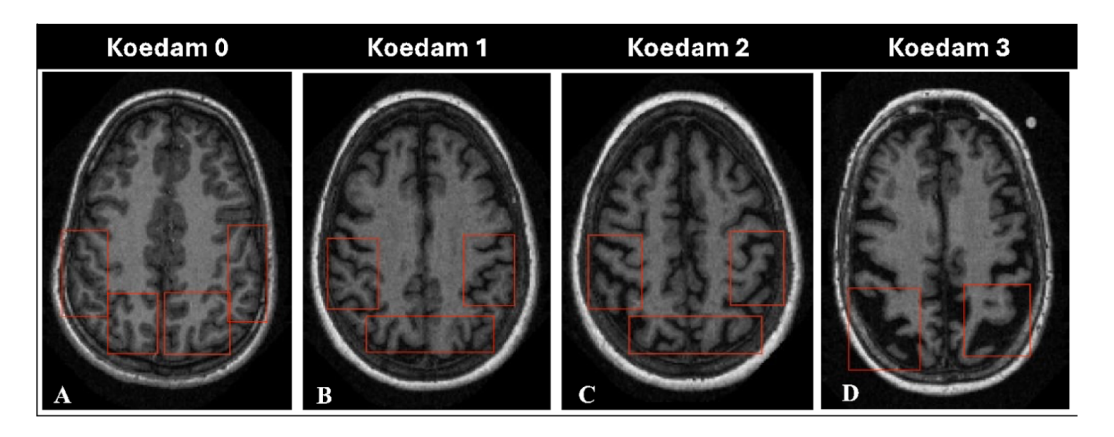


Figure 19: Axial FLAIR, coronal T1W, and sagittal T1W images with Alzheimer's disease show parietal atrophy scale.

Koedam 0: (A) shows the closed posterior cingulate, parieto-occipital, and parietal lobe sulci.

Koedam 1: (B) mild posterior cingulate, parieto-occipital, and parietal lobe sulcal widening, and the mild atrophy of precuneus.

Koedam 2: (C) substantial posterior cingulate, parieto-occipital, and the parietal lobe sulcal widening, and substantial atrophy of precuneus.

Koedam 3: (D) extremal posterior cingulate, parieto-occipital, and the parietal lobe sulcal widening, and the mild atrophy of precuneus, knife-blade precuneus atrophy.

The red bounding boxes are the signal of the Koedam scale FLAIR: Three-dimensional T2-weighted fluid-attenuated inversion-recovery imaging.

F ETHICAL STATEMENTS

F.1 COPYRIGHTS

1944

1945 1946

1947 1948

1949

1950

1951 1952

1953

1954

1957

1959

1961

1962 1963

1964 1965

1966

1967

1968 1969

1970

1971

1972

1974

1975 1976

1981

1982

1984

1987

1988

1989

1992

1993

1996

1997

F.1.1 APACHE LICENSE 2.0

The Apache License, Version 2.0 (Apache 2.0) is a **permissive open-source license** developed by the Apache Software Foundation (ASF). Its main characteristics are:

- Free Use: The software can be used for any purpose, including commercial applications.
- Modification & Distribution: Users may modify the code and redistribute original or modified versions.
- Attribution: A copy of the license must be included and proper credit given to the original authors.
- NOTICE File: If the project includes a NOTICE file, it must be preserved during redistribution.
- Patent Grant: Contributors grant users a license to patents that would otherwise be infringed by their contributions.
- Disclaimer: The license provides the software "as is" without warranties or liability.

Practical Implications:

- Permits integration into proprietary (closed-source) projects.
- Allows combination with other open-source or commercial code.
- Enables redistribution under new branding.

Restrictions:

- License and attribution notices cannot be removed.
- Modified versions cannot be misrepresented as the original work.
- Original authors cannot be held liable for issues.

F.1.2 FAIR USE

In addition to permissive open-source licenses such as Apache 2.0, the doctrine of **Fair Use** provides a legal framework that may justify the reuse of third-party datasets for research and educational purposes. Fair Use is codified under United States copyright law (17 U.S.C. §107) and is widely invoked in academic contexts, such as in our work. Its applicability is assessed through four key factors:

- Purpose and character of use: Non-commercial, educational, and research-driven usage
 is generally favored. Transformative use—where the dataset is repurposed for new scientific insights rather than replicating its original function—strengthens the case.
- 2. **Nature of the copyrighted work:** Factual and scientific data are afforded less stringent protection compared to creative works, which supports their reuse in research.
- 3. **Amount and substantiality:** Use of limited portions, or selective aspects of the dataset, weighs in favor of Fair Use. However, even large-scale use can be justified if it is essential for the research objective and transformative in nature.
- 4. **Effect on the market:** If the research use does not undermine the commercial market or value of the original dataset, this criterion supports Fair Use.

Implications for research: In practice, the reuse of existing datasets is often considered Fair Use when (i) the purpose is non-commercial and scholarly, (ii) the dataset is employed in a novel or transformative manner (e.g., re-annotating, constructing new benchmarks, or deriving insights not intended by the original authors), and (iii) proper attribution is provided.

While Fair Use is context-dependent and not absolute, adherence to these principles allows researchers to **legally and ethically justify** their use of external datasets in the advancement of science.

G LIST OF ABBREVIATIONS

ACRONYMS

1998

1999

2001				
2002		T.	L	l n
2003	Abbrev	Term	Explanation	Pages
2004	$\mathbf{A}\beta$	Beta-amyloid	Beta-amyloid is a sticky protein frag-	28–31
2005			ment that, in Alzheimer's disease, clumps together between brain cells to	
2006			form plaques that disrupt communica-	
2007			tion and damage neurons.	
2008	AD	Alzheimer's disease	Alzheimer's is a brain disease that slowly	4, 23, 28–
2009 2010			damages memory and thinking, so ev-	34
2010			eryday tasks and recognizing people be-	
2012			come harder over time.	
2013	AI	Artificial Intelligence	General term for systems that perform	3, 5, 29
2014			tasks requiring human-like intelligence	
2015	APOE	Apolipoprotein E	Apolipoprotein E (APOE) is a gene	29, 30
2016			that makes a protein helping transport fats in the brain, and its $\epsilon 4$ version	
2017			greatly increases the risk of develop-	
2018			ing Alzheimer's disease by making brain	
2019			cells more vulnerable to damage and less	
2020			able to clear toxic proteins.	
2021	CoT	Chain-of-Thought	-	1–4, 6–9,
2022				18–20, 24
2023	CSF	Cerebrospinal fluid	Cerebrospinal fluid (CSF) is a clear, wa-	28, 31
2024			tery liquid that cushions and protects the brain and spinal cord while also helping	
2025			to remove waste and deliver nutrients.	
2026	DLB	Dementia with Lewy bodies	Dementia with Lewy bodies (DLB) is a	28, 31
2027	DLD	Dementia with Lewy bodies	brain disorder where abnormal protein	20, 31
2028 2029			clumps (Lewy bodies) build up in nerve	
2029			cells, causing a mix of memory prob-	
2031			lems, movement difficulties (like Parkin-	
2032	DEL	D:00 : T :	son's), and vivid visual hallucinations.	20
2033	DTI	Diffusion Tensor Imaging	Diffusion Tensor Imaging is an MRI technique that maps how water moves	30
2034			along brain fibers, helping detect early	
2035			damage to the brain's white matter con-	
2036			nections before major memory loss or	
2037			shrinkage becomes visible.	
2038	FTD	Frontotemporal Dementia	Frontotemporal dementia (FTD) is a	28, 31
2039			brain disorder where the nerve cells	
2040			in the frontal and temporal lobes	
2041			slowly waste away, leading to early changes in personality, behavior, lan-	
2042			guage, and decision-making rather than	
2043			memory loss (which is more typical of	
2044			Alzheimer's).	
2045 2046	GCA	Global Cortical Atrophy	Global Cortical Atrophy is the	23, 28, 31,
2046			widespread shrinking of the brain's	32, 34, 35
2047			outer layer (the cortex), often linked	
2049			to aging or diseases like Alzheimer's,	
2050			which can affect memory, thinking, and behavior.	
2051	HITL	Human-In-The-Loop		23
	11111	Taman in The Loop		23

2052	Abbrev	Term	Explanation	Pages
2053	I	Koedam score	The Koedam score is a visual rating	23, 28,
2054			scale (0-3) used on brain MRI to mea-	31–34, 36
2055			sure how much the parietal cortex has	
2056			shrunk, helping to detect Alzheimer's	
2057			disease and other dementias.	
2058 2059	LLM	Large Language Model	-	1
2060	MCI	Mild Cognitive Impairment	Mild Cognitive Impairment (MCI) is a	28
2061			condition where a person has noticeable memory or thinking problems greater	
2062			than expected for their age, but not	
2063			severe enough to significantly interfere	
2064			with daily life or independent function-	
2065			ing.	
2066	MRI	Magnetic Resonance Imaging	Magnetic Resonance Imaging (MRI) is	2, 4, 28–
2067			a medical imaging technique that uses	32, 34
2068			strong magnets and radio waves to create detailed pictures of the inside of the	
2069			body without using harmful radiation.	
2070	MTA	Medial Temporal Atrophy	Medial Temporal Atrophy means the	23, 28,
2071			shrinking of memory-related brain struc-	31–33
2072			tures (like the hippocampus) in the inner	
2073			temporal lobes, often seen in aging and	
2074			Alzheimer's disease.	
2075 2076	NFT	Neurofibrillary tangles	Neurofibrillary tangles are twisted	28, 29
2077			clumps of a protein called tau that pile up inside brain cells, jam their	
2078			internal "highways," and help kill the	
2079			cells—contributing to memory loss in	
2080			Alzheimer's.	
2081	NLP	Natural Language Processing	-	1
2082	PET	Positron Emission Tomography	Positron Emission Tomography (PET) is	28, 31
2083			a medical imaging technique that uses	
2084			tiny amounts of radioactive substances to	
2085			track how organs and tissues work inside the body, creating detailed 3D pictures of	
2086			their activity.	
2087	QA	Question Answering	_	1-4, 23
2088	RAG	Retrieval-augmented Genera-	_	2, 7
2089 2090		tion		•
2090	ROI	Region of Interest	A Region of Interest (ROI) in medical	1–9, 23,
2092			imaging is simply the specific part of	34
2092			an image—like a tumor, organ, or le-	
2094			sion—that researchers mark and analyze more closely because it's the area most	
2095			relevant to diagnosis or study.	
2096	SFT	Supervised Fine-tuning	-	5, 8, 9, 18
2097	SV-	Structured Visual Chain-of-	_	2–9, 20
2098	CoT	Thought		, -
2099	VLM	Vision Language Model	_	1-3, 5-9
2100	VQA	Visual Question Answering	_	1–3, 8, 18,
2101	-	-		24–27
2102	,		•	